Geoenergy Science and Engineering, Volume 221, February 2023, Article number 211356
DOI: 10.1016/j.geoen.2022.211356

# Pore-scale modelling on complex-conductivity responses of hydrate-bearing clayey sediments: Implications for evaluating hydrate saturation and clay content

Lanchang Xing[1,*], Huanhuan Zhang[1], Shuo Wang[1], Bin Wang[1], Liyun Lao[2],

Wei Wei[3], Weifeng Han[3], Zhoutuo Wei[4,5], Xinmin Ge[4,5], Shaogui Deng[4,5]

[1] College of Control Science and Engineering, China University of Petroleum (East China), Qingdao 266580, China

[2] School of Water, Energy and Environment, Cranfield University, Cranfield MK43 0AL, UK

[3] Department of Alternative Energy, PetroChina Research Institute of Petroleum Exploration & Development, Langfang 065007, China

[4] School of Geosciences, China University of Petroleum (East China), Qingdao 266580, China

[5] Laboratory for Marine Mineral Resources, Qingdao National Laboratory for Marine Science and Technology, Qingdao 266071, China

* Correspondence: xinglc@upc.edu.cn OR l.xing@yahoo.com (Lanchang Xing)



Published by Elsevier. This is the Author Accepted Manuscript issued with: Creative Commons Attribution Non-Commercial No Derivatives License (CC:BY:NC:ND 4.0).
The final published version (version of record) is available online at DOI:10.1016/j.geoen.2022.211356. Please refer to any applicable publisher terms of use.

## Abstract

A majority of the accumulated gas hydrates exist in fine-grained unconsolidated sediments with clays, which pose challenges to reservoir evaluation with resistivity-based techniques. Characteristic electrical parameters derived from induced polarization (IP) measurements have potentials to describe complex formations of various lithology, pore-water salinities, and different depths from the borehole. However, there is still a knowledge gap in complex-conductivity properties of the hydrate-bearing clayey sediments. We present a pore-scale numerical study on modelling the low-frequency (<1 kHz) complex-conductivity spectra of clayey sediments containing hydrates based on the finite-element approach, with an emphasis on evaluating the hydrate saturation ($s_h$) and clay content. Firstly, the influences of clay type, distribution form, content and $s_h$ on the complex conductivity of sediments containing hydrates were examined systematically. Secondly, power-law and linear correlations were established for evaluating the hydrate saturation and clay content, respectively, based on complex-conductivity parameters. *(Effects of clay type)* The in-phase conductivity of hydrate-bearing smectite is significantly higher than that of hydrate-bearing illite and kaolinite due to the higher cation exchange capacity (CEC) of smectite. Higher peak frequency and quadrature conductivity appear for the hydrate-bearing kaolinite case because the mobility of counterions in the Stern layer of kaolinite is about ten times of that for smectite and illite. *(Effects of clay distribution form)* The coating-clay case has much lower in-phase and quadrature conductivities than the dispersed- and laminated-clay cases because the coating clay isolates sand particles from the pore water and no electrical double layer (EDL) forms around the sand particles. *(Effects of clay content)* With an increasing content of the structural clay up to 60%, the in-phase conductivity decreases and increases in the frequency bands lower and higher, respectively, than the peak frequency corresponding to the EDL polarization. The effective dielectric constant increases consistently with the clay content due to the much higher CEC of clays than that of sands. *(Effects of hydrate saturation)* The in-phase conductivity decreases consistently with an increasing $s_h$ up to 0.40 due to the negligible conductivity of hydrates and blockage effect on conduction currents. Both the quadrature conductivity and effective dielectric constant in the EDL-polarization-dominant frequency band decrease with an increasing $s_h$. In this work, it has been evidenced that complex-conductivity responses of hydrate-bearing clayey sediments can be understood theoretically and modelled numerically based on the interpretation of electrical conduction and electrochemical polarization mechanisms of EDLs. This study

provides a theoretical and modelling foundation for the development of new IP-based geophysical techniques for hydrate-reservoir evaluation and monitoring in both the exploration and exploitation stages.

**Keywords:** Hydrate-bearing clayey sediment, complex electrical conductivity, pore-scale modelling, hydrate saturation, clay content, finite element method

# 1 Introduction

Natural gas hydrate (NGH), which widely exists in marine sediments and land permafrost areas over the world, is a potential low-carbon-emission energy resource (Collect, 2002; Milkov, 2004; Moridis et al., 2009; Koh et al., 2012; Chong et al., 2016; Yin and Linga, 2019; Chibura et al., 2022). However, more than 90% of the accumulated global gas hydrates are hosted in fine-grained unconsolidated sediments, such as those in the Gulf of Mexico, Krishna-Godavari basin, Blake Ridge, Cascadia Margin, Ulleung Basin, Hydrate Ridge and South China Sea (Boswell, 2009; Boswell and Collett, 2011; Dai et al., 2011; Liu et al., 2012; Sriram et al., 2014; Jang and Santamarina, 2016; Boswell et al., 2020; Park et al., 2022). To achieve the ultimate goal of NGH development from the unconsolidated clayey-silty sediments, at present, it is an urgent task to develop a suite of safe and efficient exploration and exploitation techniques (Ye et al., 2020; Sahu et al., 2020; Liu and Li, 2021; Mao et al., 2021; Shi et al., 2021; Zhu et al., 2021; Wei et al., 2022). The hydrate saturation is a basic reservoir parameter, which is widely used for estimating the amount of gas resources, predicting the permeability of formations and designing production strategies. Unfortunately, the complexity of hydrate-bearing sediments (HBS) pose various challenges to a reliable and accurate estimation of hydrate saturation, especially for clayey sediments. It is a highly desirable undertaking to develop new geophysical techniques to evaluate the hydrate saturation in hydrate-bearing clayey sediments.

The influences of clays on hydrate formation/decomposition characteristics and physical/chemical properties of hydrate-bearing sediments have attracted extensive research works recently (Wu et al., 2021). Yun et al. (2007) and Lee et al. (2010a) explored large/intermediate/small-strain mechanical properties of THF-hydrate-bearing sand, silt, and clay with various hydrate saturations. It was revealed that the high specific surface area (SSA) induced by clays is one of the governing factors to the strength and cementation parameters as well as the acoustic velocities. Kumar et al. (2015) investigated the formation kinetics of methane hydrate in porous materials of various ratios of silica sand and clay. They observed that the presence of fine clay particles hindered the effective mass transfer of gases used for hydrate formation, and resulted in a decreased hydrate conversion rate. Han et al. (2016) conducted experimental investigations on the sediment deformation over the course of methane-hydrate dissociation in both sandy and silty sediments. It was demonstrated that the hydrate

decomposition conditions in silty clay sediments shifted into the region with a higher pressure than that in sandy sediments due to the smaller particle sizes. In the work of Jang and Santamarina (2016), they considered the hydrate-bearing clayey sediment as a two-material system. In this system, the segregated hydrate was surrounded by the water-saturated clay with no hydrate. It was stressed that the high SSA and small pore size induced by clay determines the permeability and capillarity of hydrate-bearing clayey sediments. The phase equilibrium boundary between the hydrate and gas/water could be altered for pores smaller than 100 nm with an addition of even a small amount of clay into sandy sediments. Zhan et al. (2018) simulated hydrate-bearing sediments with quartz sands of different particle sizes ranging from 37 to 350 μm and performed hydrate formation and decomposition experiments. It was shown based on the experimental analysis that the rates of hydrate formation and gas production decreased with the particle size. Moreover, the sediments of smaller particle sizes produced more significant deformations in the process of hydrate decomposition. Liu et al. (2019) visualized the microscale distribution and morphology of hydrates using X-ray CT, and used elastic waves to characterize clayey sediments containing hydrates. It was demonstrated that the THF hydrate formed in clays exhibited a segregated mode, which acted as inclusions in the clayey matrix. Their results invalidated the rock-physics models based on an assumption that the hydrate acted as a pore constituent. To summarize, the above works have shown the significant influences of clays on the mechanical properties of HBS, hydrate formation/dissociation kinetics and conditions, hydrate distribution and morphology in sediments.

In terms of the electrical properties of HBS, theoretically, both the electrical conduction and polarization characteristics of hydrate-bearing sediments can be influenced significantly by clays due to their high SSA, water sensitivity property and excess surface charges (induced by the high cation exchange capacity, CEC). Therefore, it is of essential importance to explore the clay effects on the electrical properties of HBS and develop clay-correction models to achieve a reliable evaluation of hydrate saturation. Based on the assumption that the effects of hydrate formation in pores can be approximated as a reduction of porosity, the standard Archie and corrected Archie relationships have been adopted to predict the hydrate saturation for clayey sediments (Hyndman et al., 1999; Collett and Ladd, 2000; Riedel et al., 2005; Riedel et al., 2006; Lee and Collett, 2009; Shankar and Riedel, 2011; Wang et al., 2011ab; Riedel et al., 2013). Miyairi et al. (1999) conducted an interpretation of the resistivity logging data from the Mallik 2L-38 well by using the Indonesian equation. In

this electrical-resistivity method, an explicit correction term accounting for the effect of shale conductivity was added into the Archie's equation. Lee et al. (2010b) measured the conductivity and permittivity of hydrate-bearing sand, silt, and clay sediments at frequencies ranging from 0.2 to 1.3 GHz in laboratory. Due to the ignorance of the surface conductance in a high SSA sediment, it was less reliable to estimate the hydrate saturation by using the measured conductivity and Archie-type relationships. In the work of Lee and Collet (2006, 2011), they employed the Simandoux model to correct for the clay-conduction effects on the resistivity of formations. Lee (2011) modified the connectivity equation (CE) to correct for the effects of clays. The modified-CE method was recommended due to its simplicity and comparable saturation-estimation results with the Waxman and Smits method (Waxman and Smits, 1968) based on the interpretation of laboratory and field-logging data. Generally, the Archie-type models are more applicable to sediments with lower clay contents and higher porosities. Meanwhile, the above clay-correction models (e.g., Indonesian, Simandoux equations) require some additional or empirical parameters. It is still a challenge to determine those parameters accurately. It also needs to be noted that only the clay content is taken into consideration while the distribution forms exhibited by clay minerals in sediments are ignored. In order to address the above issues related to the clay correction models and clay distribution forms, Hu et al. (2019) employed the effective medium theory (EMT) and established two different resistivity models for evaluating the hydrate saturation under different distribution forms of clays. The effectiveness of the models was demonstrated by using the resistivity measurements from core samples and logging data. However, only two distribution forms, i.e., dispersed and laminated, were taken into consideration due to the limit of the specific studied area of Qilian Mountain permafrost. More clay-distribution forms such as the structural and coating clay may exist in hydrate-bearing marine sediments (de Lima and Sharma, 1990; Okay et al., 2014; Revil et al., 2015). In addition, the SSA, CEC and water sensitivity property of clay minerals vary greatly depending on the types of minerals such as smectite, illite and kaolinite. Therefore, a systematic investigation of the clay effects in terms of the mineral types, content and distribution forms on the electrical properties of sediments containing hydrates is a highly desirable undertaking.

Geophysical logging techniques frequently used in oil and gas engineering have been playing a key role in the identification, assessment and monitoring of hydrate-bearing formations. The conventional resistivity logging has become an indispensable means for evaluating the hydrate-reservoir parameters such as porosity, saturation,

and permeability (Hyndman et al., 1999; Collett and Ladd, 2000; Riedel et al., 2005; Shankar and Riedel, 2011; Wang et al., 2011ab; Riedel et al., 2013; Cook and Waite, 2018). Recently, various correlations between the resistivity and hydrate saturation have been proposed based on numerical simulations and experiments (Dong et al., 2019; Jin et al., 2020; Zhang et al., 2021). However, severe problems arise due to the particularity of the unconsolidated clayey sediments containing hydrates. Firstly, the decomposition and subsequent reformation processes of hydrates result in unpredictable variations of the pore-fluid salinity in response to the release and consumption of fresh water in the two processes, respectively (Ning et al., 2013ab; Santamarina et al., 2015; Yang et al., 2019). Secondly, the clay minerals vary the lithology and influence the physical/chemical properties of sediments significantly. The approach of complex-resistivity logging was proposed by introducing the induced polarization (IP) principle to boreholes from the ground-surface survey (Worthington and Collar, 1984; Freedman and Vogiatzis, 1986; Osterman et al., 2016). It has been reported that some characteristic parameters derived from the frequency-dispersive spectra of complex resistivity/conductivity can be related to reservoir parameters quantitatively, and these relationships are insensitive to variations of the pore-water salinity of formations (Jiang et al., 2018a; Li et al., 2019). Furthermore, the information of formations with different depths from the borehole can be acquired by applying the complex-resistivity logging method, because a range of frequencies of the excitation electric fields are usually utilized when measuring the complex-conductivity spectra. Bearing the merits of the borehole IP method in mind, we believe that more understandings of the electrical properties of hydrate-bearing clayey sediments could be obtained from a variety of complex-conductivity parameters. Moreover, the complex-conductivity method based on the IP principle may possess potentials for evaluating hydrate-bearing clayey sediments quantitatively.

To date, the parameters for characterizing electrical properties of hydrate-bearing clayey sediments have been restricted to the resistivity/conductivity and high-frequency dielectric permittivity (i.e., based on molecular polarization mechanism). There is still a lack of works on characterizing the low frequency (e.g., <1 kHz) permittivity properties (i.e., controlled by the EDL polarization mechanism) of hydrate-bearing clayey sediments. A fully understanding of the low-frequency electrical properties is an essential first step to utilize the IP/complex-conductivity method for hydrate-reservoir evaluation. The objective of this work is to present a pore-scale numerical approach for modelling the complex-conductivity spectra of clayey sediments containing

hydrates, and characterize the effects of clays with an emphasis on the evaluation of hydrate saturation and clay content. Firstly, theoretical formulations are derived within the framework of low-frequency electrical polarization mechanism, which provides a theoretical basis for the pore-scale numerical modelling. Secondly, finite-element based numerical models of hydrate-bearing clayey sediments are constructed and complex-conductivity responses are obtained numerically under conditions of different clay types, clay contents, clay distribution forms, and hydrate saturations. Thirdly, the effects of clays are analyzed and quantified, and then correlations for evaluating the clay content and hydrate saturation are established. This is followed by discussions and conclusions.

# 2 Theoretical basis

## 2.1 Complex electrical conductivity of hydrate-bearing porous media

There are two electrical processes, i.e., directional migrations of the free-moving charges, as well as displacements of the bound charges, for a medium with an electric field applied. The former process is controlled by the electrical conduction mechanism, which can be described by electrical conductivity. While the electrical polarization mechanism, which can be characterized by dielectric permittivity, controls the latter process. An alternating electrical field (denoted as **E**) results in a total current density, which can be calculated by summing up conduction and displacement current densities as shown in Eq. (1) based on the Ohm's law and the first Maxwell equation (Tarasov and Titov, 2013).

$$\mathbf{J}=\mathbf{J_c}+\mathbf{J_d}=\sigma\mathbf{E}+\mathrm{i}\omega\varepsilon\mathbf{E} \tag{1}$$

where $\mathbf{J}$, $\mathbf{J_c}$, and $\mathbf{J_d}$ are the total, conduction and displacement current densities (in A/m$^2$), respectively, and $\sigma$ (in S/m) and $\varepsilon$ (in F/m) denotes the electrical conductivity and dielectric permittivity, respectively. The intensity $\mathbf{E}$ normally takes a harmonic form, i.e., $\mathbf{E} = \mathbf{E_0}e^{i\omega t}$, where $\omega$ (in rad/s) is the angular frequency (i.e., $\omega = 2\pi f$, $f$ in Hz), and $\mathbf{E_0}$ is an electrical field of constant magnitude and direction. Treating the electrical conductivity to be a complex number (denoted as $\sigma^*$, complex conductivity), the total current density ($\mathbf{J}$) can be rewritten as Eq. (2) taking the form of Ohm's law.

$$\mathbf{J}=\sigma^*\mathbf{E} \tag{2}$$

where the complex conductivity ($\sigma^*=\sigma+\mathrm{i}\omega\varepsilon$) characterizes the electromigration mechanism of charges and

electrical polarization mechanism, $\sigma = \sigma' + \mathrm{i}\sigma''$ and $\varepsilon = \varepsilon' + \mathrm{i}\varepsilon''$ are frequency-dependent complex scalars. The complex conductivity can be alternatively formulated in terms of the effective complex conductivity ($\sigma^*_{eff}$).

$$\sigma^* = \sigma^*_{eff} = \sigma_{eff} + \mathrm{i}\omega\varepsilon_{eff} \tag{3}$$

where $\sigma_{eff} = \sigma' - \omega\varepsilon''$ and $\varepsilon_{eff} = \varepsilon' + \sigma''/\omega$ denote the effective conductivity (in S/m) and effective permittivity (in F/m), respectively. Both of them are frequency-dependent real scalars that can be obtained directly from experimental or field measurements.

In a low frequency range (typically <10 kHz), several analytical models have been proposed to reproduce the complex-conductivity responses of sands and clayey materials (Leroy et al., 2008; Revil and Florsch, 2010; Schmutz et al., 2010; Revil, 2012; Revil et al., 2013). In addition, Revil (2013) reported a model accounting for the low-frequency electrochemical polarization mechanism of the Stern layer (i.e., the inner part of EDL) for unsaturated porous materials with water and air as the wetting and non-wetting phase, respectively. By substituting the air phase with hydrate, the complex conductivity (denoted as $\sigma^*$) of hydrate-bearing porous media can be computed with the pore-water conductivity ($\sigma_w$) and complex-valued surface conductivity ($\sigma^*_s$) of mineral grains.

$$\sigma^* = \frac{1}{F}\left[ s_w^n \sigma_w + (F-1)\sigma_s^* \right] \tag{4}$$

where $F$ denotes the formation factor, $n$ represents the saturation exponent, $\sigma^*_s = \sigma'_s + \mathrm{i}\sigma''_s$ is the complex-valued surface conductivity due to the EDL coating the solid phase (i.e., mineral grains), and $s_w$ denotes the saturation of water ($s_w + s_h = 1$, where $s_h$ is the hydrate saturation.). The formation factor can be related to the porosity (denoted as $\varphi$) based on the Archie's formula (Archie, 1942), i.e., $F = \varphi^{-m}$, where $m$ is the cementation exponent.

## 2.2 In-phase conductivity of unsaturated porous media

In the cases of hydrate-bearing porous media with the mineral grains in contact to each other, it is assumed that

only the conduction of the diffuse layer contributes the low-frequency surface conductivity. As a result, the low-frequency (in-phase) conductivity of the solid mineral phase (i.e., $\sigma_s^0$) is given by a function as formulated in Eq. (5). It can be seen that $\sigma_s^0$ can be obtained with known surface charge density in the diffuse layer (denoted as $Q_d$, in C/m$^2$), mobility of counterions in the diffuse layer (denoted as $\beta_{(+)}$, in m$^2$/(sV)), and tortuosity of electromigration paths along the mineral surface in water phase (denoted as $\alpha_w$, dimensionless).

$$\sigma_s^0 = \frac{\beta_{(+)}}{\alpha_w} Q_d \frac{S}{V_s} \tag{5}$$

where $S$ (in m$^2$) represents the surface area of the mineral grains, $V_s$ (in m$^3$) is the volume of the mineral grains, and $Q_d$ can be represented by CEC. Then the low-frequency surface conductivity for unsaturated cases (e.g., with the hydrate saturation $s_h = 1 - s_w$) can be given by

$$\sigma_s^0 = \frac{s_w^p}{F\varphi} \beta_{(+)} \left(1 - f_{pc}\right) \rho_s \mathrm{CEC} \tag{6}$$

where $\rho_s$ (in kg/m$^3$) represents the density of solid mineral grains, and $f_{pc}$ is the partition coefficient, which represents the relative count fraction of counterions in the Stern layer to those in EDL. As a result, the count fraction of counterions in the diffuse layer can be represented by $(1 - f_{pc})$. The term $s_w^p / F\varphi$ accounts for effects of the water saturation and tortuosity, where $p$ ($p \approx n - 1$) is usually used instead of $(n - 1)$ to differentiate the true tortuosity of pathways along grains from that of the water phase adjacent to the grains. The high-frequency surface conductivity (i.e., $\sigma_s^\infty$) can be derived by incorporating contributions from the whole EDL as formulated in Eq. (7).

$$\sigma_s^\infty = \frac{s_w^p}{F\varphi} \left[ \beta_{(+)} \left(1 - f_{pc}\right) + \beta_{(+)}^S f_{pc} \right] \rho_s \mathrm{CEC} \tag{7}$$

where $\beta_{(+)}^S$ (in m$^2$/(sV)) denotes the mobility of counterions in the Stern layer. It has been reported that $\beta_{(+)}^S \ll \beta_{(+)}$ for clays (Revil, 2012) and $\beta_{(+)}^S = \beta_{(+)}$ for silica sands (Revil et al., 2012b).

By substituting $\sigma_s^0$ and $\sigma_s^\infty$ into Eq. (4), the low- and high-frequency electrical conductivities (denoted as $\sigma^0$ and $\sigma^\infty$, respectively) of the unsaturated porous media containing hydrates can be expressed as Eqs. (8) and (9), respectively.

$$\sigma^0 = \frac{1}{F}\left[ s_w^n \sigma_w + (F-1)\frac{s_w^p}{F\varphi}\beta_{(+)}(1-f_{pc})\rho_s \mathrm{CEC} \right] \tag{8}$$

$$\sigma^\infty = \frac{1}{F}\left\{ s_w^n \sigma_w + (F-1)\frac{s_w^p}{F\varphi}\left[ \beta_{(+)}(1-f_{pc}) + \beta_{(+)}^S f_{pc} \right]\rho_s \mathrm{CEC} \right\} \tag{9}$$

Substituting the relationship CEC = $Q_s S_{sp}$ into Eqs. (8) and (9), the above conductivities can be expressed as a function of the SSA (denoted as $S_{sp}$, in $m^2/kg$) instead of the CEC, where $Q_s = Q_d/(1–f_{pc})$ is the mean charge density for the solid phase.

## 2.3 Complex surface conductivity for different types of clay minerals

The porous media involved in this work are hydrate-bearing clays and clayey sands with various types of clay minerals at different saturations of hydrates in the fluid-suspending mode (Xing et al., 2021; Hu et al., 2022). As reported in the works such as Ma et al. (2020), Liu and Li (2021) and Ren et al. (2022), three types of clay minerals including kaolinite, illite and smectite dominate the shale component in natural hydrate-bearing sediments. Due to the large differences in CEC and SSA among the three types of clay mineral, two sets of formulations have been proposed for modelling the complex surface conductivity for kaolinite and smectite/illite, respectively (Leroy and Revil, 2009).

For modelling the complex conductivity of clayey materials, Leroy and Revil (2009) related the electrochemical properties of clay minerals with the spectra of effective electrical conductivity and dielectric permittivity. In the case of kaolinite particles, it is considered that the diffuse layer only occupies a minor part of the pore space due to the lower SSA of this mineral. Consequently, the diffuse layer only influences the effective conductivity of the solid mineral particles. For the case that the porous material includes only kaolinite or sand particles with the same size, the complex surface conductivity is then given by Eq. (10) for saturated cases.

$$\sigma_s^*(\omega) = \sigma_s^\infty - \frac{\sigma_s^\infty - \sigma_s^0}{1+\omega^2\tau_p^2} + \mathrm{i}\frac{(\sigma_s^\infty - \sigma_s^0)\omega\tau_p}{1+\omega^2\tau_p^2} \tag{10}$$

$$\sigma_s^0 = \frac{2}{\Lambda}\Sigma_s^0 \tag{11}$$

$$\sigma_s^\infty = \frac{2}{\Lambda}\left(\Sigma_s^0 + \Sigma_s^\infty\right) \tag{12}$$

where $\tau_p = 1/(2\pi f_{peak})$ (in s) represents the characteristic relaxation time, and $f_{peak}$ denotes the corresponding critical frequency (i.e., the peak frequency in this work). Based on the assumption that the EDL polarization mechanism dominates the low-frequency polarization processes, the characteristic relaxation time ($\tau_p$) can be calculated by Eq. (13) for unsaturated porous media with the water saturation of $s_w$.

$$\tau_p = \frac{\Lambda^2}{2D_{(+)}^S} s_w^2 \tag{13}$$

where $\Lambda$ denotes the characteristic pore/throat size (i.e., the dynamic pore radius, in m), and $D_{(+)}^S$ (in $m^2/s$) represents the diffusing coefficient of counterions in Stern layer. A relationship between $F$, $\Lambda$ and grain diameter ($d$ in m) as formulated in Eq. (14) has been developed by Revil and Cathles (1999) for an ideal granular material. This material is composed of grains with a spherical shape and the same diameter.

$$\Lambda = \frac{d}{2m\left(F-1\right)} \tag{14}$$

The parameters $\sum_s^0$ and $\sum_s^\infty$ (in S) represent the specific surface conductivities attributed to the diffuse and Stern layers, respectively, which are calculated by using Eqs. (15) and (16), respectively.

$$\Sigma_s^0 = \beta_{(+)} e \Gamma_{(+)}^d + \Sigma_s^0(\mathrm{H}^+) \tag{15}$$

$$\Sigma_s^\infty = \beta_{(+)}^S e \Gamma_{(+)}^{S0} \tag{16}$$

where $\Gamma_{(+)}^d$ and $\Gamma_{(+)}^{S0}$ (in counterions/$m^2$) denote the surface site densities of counterions in EDL (i.e., for the diffuse layer and the Stern layer, respectively), $\Sigma_S^0(\mathrm{H}^+)$ is attributed to the protons of water adsorbed on the solid particles, and $e$ represents the elementary charge (i.e., $e = 1.602\times10^{-19}$ C).

In cases of smectite and illite particles with low pore-fluid salinity (e.g., < 0.01 mol/L), it is believed that the diffuse layer on solid mineral particles remains continuous at the pore-space scale. Consequently, only the polarization of Stern layer is taken into account rather than the whole EDL. The complex-valued surface conductivity for this case is formulated as Eq. (17).

$$\overline{\sigma}_s^*(\omega) = \frac{(\sigma_s^\infty - \sigma_s^0)\omega^2\tau_p^2}{1+\omega^2\tau_p^2} + \mathrm{i}\frac{(\sigma_s^\infty - \sigma_s^0)\omega\tau_p}{1+\omega^2\tau_p^2} \tag{17}$$

It needs to be noted that only the contribution of Stern layer to the electrical conductivity has been included in

Eq. (17). While the diffuse layer is taken into account by replacing the term $\sigma_w$ in pore space with an effective pore-water conductivity. Based on the assumption that one type of cation (e.g., $Na^+$, $K^+$) is the dominant ionic species, the effective pore-water conductivity ($\overline{\sigma}_w$) in these cases can be approximated as below:

$$\overline{\sigma}_w \approx \beta_{(+)} \overline{Q}_V \tag{18}$$

where $\overline{Q}_V$ is the volumetric charge density (in C/m$^3$) in the pore water. It can be related to the total bulk charge density (denoted as $Q_V$) by using $f_{pc}$ as shown in Eq. (19) (Revil et al., 2012a). The $Q_V$ can be related to CEC as formulated in Eq. (20).

$$\overline{Q}_V = \left(1 - f_{pc}\right) Q_V \tag{19}$$

$$Q_V = \rho_s \left( \frac{1-\varphi}{\varphi} \right) \mathrm{CEC} \tag{20}$$

For the cases of hydrate-bearing clayey sands including both clay minerals and sands, the complex surface conductivities of sand grains and clay particles can be calculated by a combination use of Eqs. (10) and (17). Eq. (10) is applicable to cases with sands or kaolinite, while Eq. (17) applies to smectite and illite cases.

# 3 Numerical modelling with finite element method

## 3.1 Scheme of numerical modelling

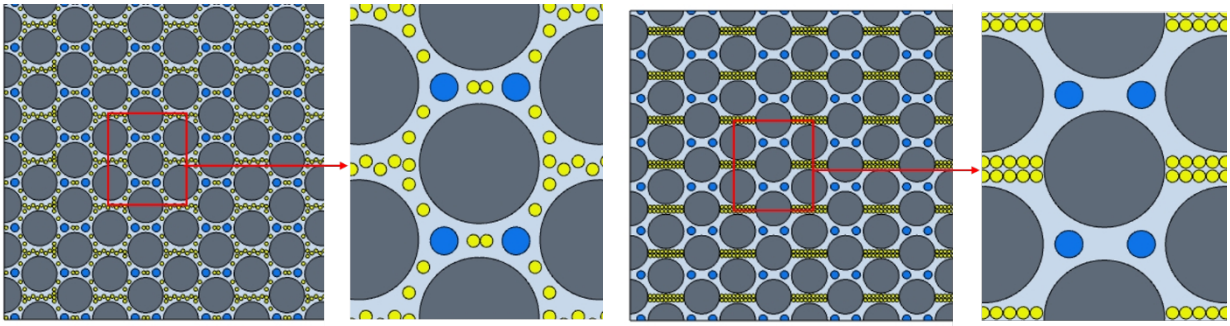
A finite-element modelling scheme is designed to obtain the electrical responses in terms of complex-conductivity spectra of hydrate-bearing clayey sands. The scheme includes three steps, i.e., construction and meshing of computational domains representing hydrate-bearing clayey sands, calculation and designation of electrical properties of the involved materials (e.g., the hydrate, clay, pore water, sand grains etc.), determination and solution of electric-field equations.

We have built two-dimensional (2D) computational domains for modelling hydrate-bearing clayey sands (i.e., analogue to the representative elementary volume in 3D models, REV). The solid phases including hydrate clusters, clay particles and sand grains are represented by circular surfaces. They are differentiated by an appropriate designation of the corresponding electrical properties (i.e., the effective conductivity and permittivity). Different hydrate saturations, micro-distribution modes of hydrate, and clay distribution forms

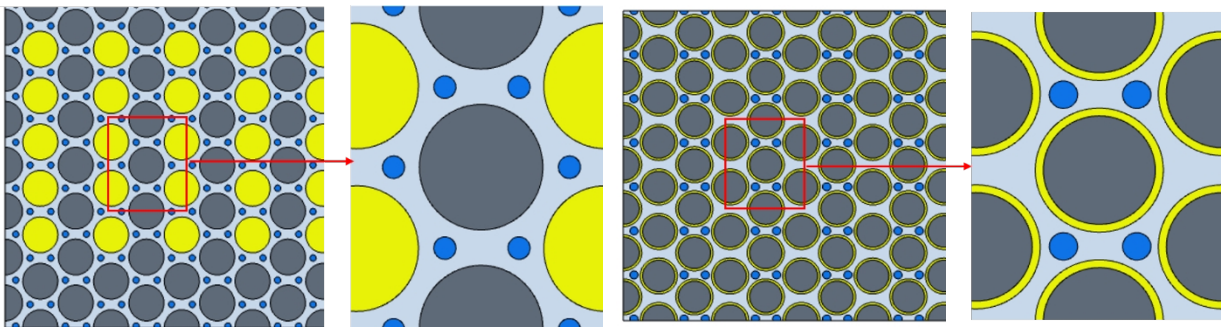
can be achieved by manipulating the areas and locations of the circular surfaces. The finite element approach is employed to solve the equations of the electric-field model, through which numerical solutions to the current through the REV representing hydrate-bearing clayey sediments can be obtained. The complex-conductivity spectra of the REVs can then be derived from the numerical solutions. The commercial platform COMSOL Multiphysics (v5.6) is adopted to realize the scheme of finite-element modelling in this work.

### 3.2 Construction of computational domains

A series of 2D computational domains are constructed to model hydrate-bearing clayey sands with various hydrate saturations, clay contents and distribution forms of clays for hydrates in a fluid-suspending mode. As shown in **Fig. 1**, four components including the sand grains, clay particles, hydrate clusters and pore water are taken into consideration in the computational domains. Four distribution forms of clays, i.e., dispersed clay, laminated clay, structural clay and coating clay, are modelled in this study with a reference to the works such as de Lima and Sharma (1990), Okay et al. (2014), Revil et al. (2015), and Hu et al. (2019).



(a) Dispersed clay (b) Laminated clay



(c) Structural clay (d) Coating clay

**Fig. 1 Computational domains for hydrate-bearing clayey sands with various distribution forms of clays (Blue: hydrate; Yellow: clay; Dark gray: sand; Light gray: pore water)**

The length and width of the 2D rectangular geometries are 0.432 mm and 0.216 mm, respectively. A number of circular surfaces are allocated evenly or in a certain distribution style in the geometries. The circular surfaces representing sand grains are distributed evenly in the rectangular computational domain. The diameter of the sand grains remains to be constant, i.e., 24 μm for the 142 circular surfaces. The sands of this size can be grouped into silt representing the fine marine sediments containing hydrates (Shepard, 1954; Sun et al., 2012; Liu et al., 2012). An effective porosity of 0.40 is obtained at conditions without any hydrate and clay in the geometry. The hydrate saturation is varied through an adjustment of the diameter for the circular surfaces representing hydrate clusters. In the case of dispersed clay as shown in **Fig. 1 (a)**, the circular surfaces representing clays are distributed evenly in the pores. Different clay contents can be realized by varying the diameter of the corresponding circular surfaces. Layers of clay particles represented by small-diameter circular surfaces are allocated in the pores for the laminated clay case as presented in **Fig. 1 (b)**. **Fig. 1 (c)** demonstrates that a certain number of sand grains are displaced by clay particles in the structural clay case. In the coating clay case, the clay component coats the surface of sand grains as shown in **Fig. 1 (d)**.

### 3.3 Physical properties of materials

As indicated in the above sections there are four components in the computational domains. Therefore, four materials in the numerical models have to be defined by using the electrical properties, i.e., the electrical conductivity and dielectric permittivity. Considering the low-frequency polarization mechanism of EDL, effective electrical parameters resulting from the surface conductance of sand grains and clay particles are required to be computed first. The effective conductivity and permittivity can be calculated through Eq. (21) for the surface conductivity. Then the effective electrical parameters are assigned to the sand grains and clay particles in the models. A very low electrical conductivity (e.g., $10^{-5}$ S/m) is assigned to the hydrate (du Frane et al., 2011), and the dielectric permittivity is specified as $60\varepsilon_0$ ($\varepsilon_0 = 8.854 \times 10^{-12}$ F/m, i.e., the dielectric permittivity in vacuum) at the low frequencies (Waite et al., 2009; Haukalid et al., 2017). The pore-fluid conductivity is computed by Eq. (22) to take the effects of temperature and salinity into account (Sen and Goode, 1992), while the dielectric permittivity takes a constant value of $80\varepsilon_0$. The dielectric permittivity of the pore fluid and hydrate remains unchanged over the frequency range involved in this work. This is reasonable because

the mean values and variations of the permittivity are much smaller than the effective permittivity of clay particles or even sand grains coated with polarizable EDLs at low frequencies (refer to the results in **Section 4**).

$$\begin{cases} \sigma_{eff} = \sigma_s^{'} \\ \varepsilon_{eff} = \sigma_s^{''} / \omega \end{cases} \tag{21}$$

$$\sigma_w = \left[ 5.6 + 0.27\left(T - 273.15\right) - 1.5 \times 10^{-4}\left(T - 273.15\right)^2 \right] C_f - \left[ \frac{2.36 + 0.099\left(T - 273.15\right)}{1.0 + 0.214 C_f} \right] \left(C_f\right)^{3/2} \tag{22}$$

where $T$ is the temperature (in K), and $C_f$ represents the pore-water salinity (in mol/L).

### 3.4 Mesh and solution

The 2D computational domain including components such as sand grains, clay particles, hydrate clusters and pore water is discretized into triangular elements for model solving based on the finite element approach. The dependency of model solutions on mesh size is examined in order to select an appropriate size level. A proper mesh level is finally selected based on a tradeoff between the computation time and model accuracy.

To obtain frequency-dispersion characteristics of complex conductivity, a range of frequencies is covered for the sinusoidal electrical potential applied on the boundary of the computational domain. The frequency of the applied electric potentials ranges from $10^{-5}$ to $10^{6}$ Hz. This is realized by sweeping the excitation frequency in the FE models. The complex conductivity of the computational domains, i.e. the modelled REVs, is obtained by dividing the applied potential by the resultant current. As there is a phase difference between the applied electric potential and resultant current due to the electrical polarization mechanism, a complex-valued electrical conductivity is often involved in the computation process for solving model equations.

## 4 Results

### 4.1 Validation of numerical models

As a benchmark case, a model of the water-saturated kaolinite has been constructed and meshed at different size levels. **Table 1** gives the parameters of the meshes used in the example case. The models with a variety of mesh sizes are solved numerically to examine the size effects on model solutions. Variations of the quadrature

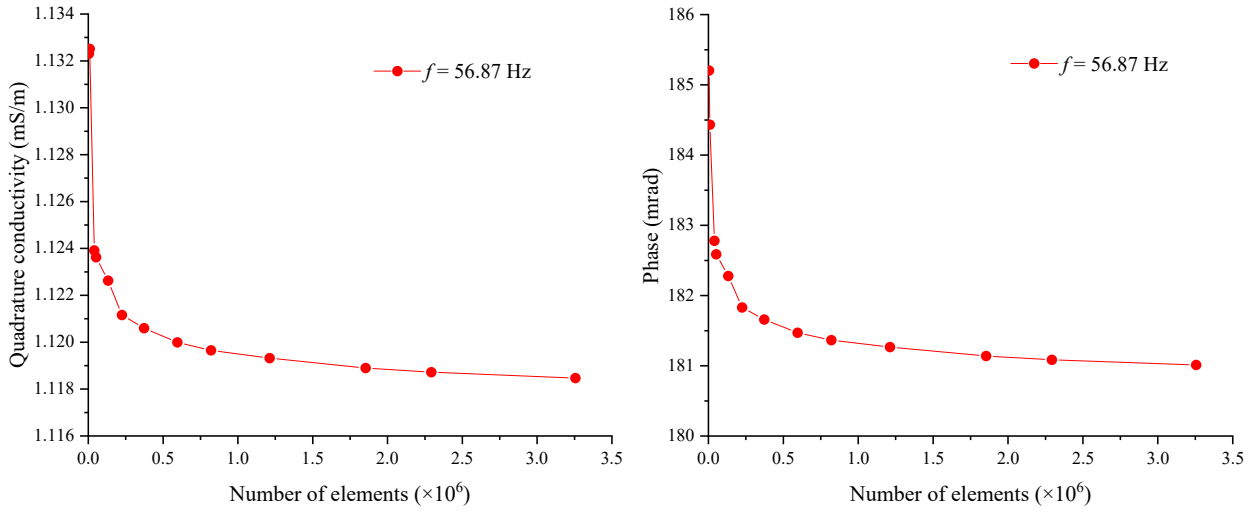
conductivity and phase angle with the count of elements are shown in **Fig. 2**. Through an examination of the variation trends of the two complex-conductivity parameters, a proper level of mesh sizes are selected for the numerical modelling cases in the rest of this work. Both the shown parameters of complex conductivity in **Fig. 2** converge to steady values with an increasing element number, i.e. a decreasing mean size. To balance the two aspects, i.e., the accuracy of model solutions and computational cost, it has been determined to use the mesh that comprises of 820,650 elements for further numerical modelling. The element size for the selected mesh ranges from 0.6 $\mu$m to $8.64\times10^{-3}$ $\mu$m.

**Table 1 Meshes used for mesh-dependency examination**

| Mesh level | Minimum element size (mm) | Maximum element size (mm) | Count of elements |
|---|---|---|---|
| 1 | $2.16\times10^{-2}$ | $1.43\times10^{-1}$ | 3774 |
| 2 | $6.91\times10^{-3}$ | $8.64\times10^{-2}$ | 9370 |
| 3 | $2.59\times10^{-3}$ | $5.62\times10^{-2}$ | 38609 |
| 4 | $8.64\times10^{-6}$ | $4.32\times10^{-3}$ | 51780 |
| 5 | $8.64\times10^{-6}$ | $1.50\times10^{-3}$ | 132427 |
| 6 | $8.64\times10^{-6}$ | $1.20\times10^{-3}$ | 224753 |
| 7 | $8.64\times10^{-6}$ | $0.90\times10^{-3}$ | 372286 |
| 8 | $8.64\times10^{-6}$ | $0.70\times10^{-3}$ | 595372 |
| 9 | $8.64\times10^{-6}$ | $0.60\times10^{-3}$ | 820650 |
| 10 | $8.64\times10^{-6}$ | $0.50\times10^{-3}$ | 1212235 |
| 11 | $8.64\times10^{-6}$ | $0.40\times10^{-3}$ | 1853450 |
| 12 | $8.64\times10^{-6}$ | $0.36\times10^{-3}$ | 2392537 |
| 13 | $8.64\times10^{-6}$ | $0.30\times10^{-3}$ | 3255722 |

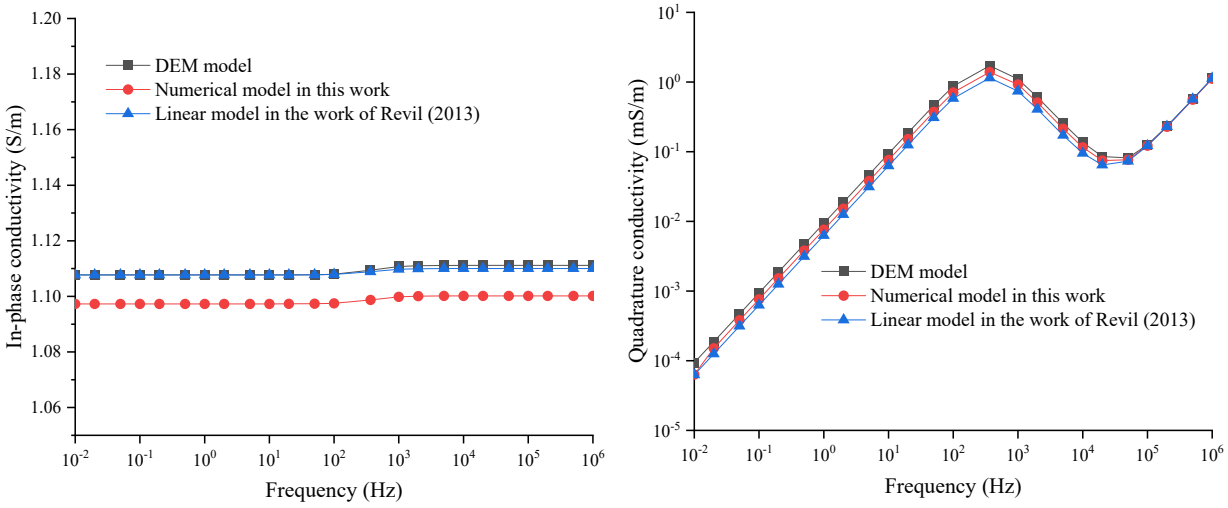
An example model of a water-saturated smectite (a representative of clay minerals) is constructed and solved numerically based on the selected level of mesh. To further validate the modelling scheme presented above, the model solution of complex conductivity is compared with those from the differential effective medium (DEM) model (Niu and Zhang, 2017; Kim et al., 2022) and the linear model presented by Revil (2013). **Fig. 3** presents the complex conductivity in terms of frequency-dispersive spectra of in-phase and quadrature conductivities. It has been clearly demonstrated that the solutions from this numerical model coincide with those from the DEM model and Revil's model quite well. The deviation of the in-phase conductivity obtained from this numerical

model is less than 1.0 % compared with the other two solutions. For the quadrature conductivity, the numerical solution is located in the middle of those two solutions. The quadrature conductivity exhibits a clear peak in the frequency spectrum, which is located between 0.1 kHz and 1.0 kHz in this example case. The frequency at which the quadrature conductivity reaches a peak (i.e., the maximum as shown in **Fig. 3(b)**) is the peak frequency used in this work. It can be computed by $f_{peak} = 1/(2\pi\tau_p) \approx 358$ Hz for this example case, which can be related to the characteristic pore/throat size and diffusing coefficient of the counterions in Stern layer (refer to Eq. (13). The $f_{peak}$ defines the upper limit of the lower frequency band, in which the electrochemical polarization mechanism of EDLs that coat the solid grains including sand or clay particles controls the polarization processes.




(a) Quadrature conductivity (b) Phase angle

**Fig. 2 Evolution of the complex-conductivity parameters with the element count for a variety of size levels**




(a) In-phase conductivity (b) Quadrature conductivity

**Fig. 3 Comparison of the complex-conductivity spectra from the DEM model, model of this work and Revil's model (Revil, 2013)**

## 4.2 Effects of clay type

Three typical types of clay minerals such as kaolinite, illite, and smectite dominate the shale component in hydrate-bearing clayey sediments as indicated by the analysis of cores retrieved from field drilling (Ma et al., 2020; Liu and Li, 2021; Ren et al., 2022). There are significant differences in CEC, SSA, source of excess surface charge, and interlayer force among them. Consequently, it is reasonable that the complex-conductivity responses of hydrate-bearing sediments with different types of clays exhibit different characteristics. In this section, we consider hydrate-bearing clays with different types of clay minerals, and compute complex conductivities through the numerical modelling approach. Six typical cases including the three types of clay minerals and two pore-water salinities are designed and key parameters are presented in **Table 2**. **Fig. 4** and **Fig. 5** show the complex-conductivity spectra for the test cases, where the in-phase conductivity, quadrature conductivity and effective dielectric constant for the three types of hydrate-bearing clays with different pore-water salinities are included. The effective dielectric constant (denoted as $\kappa_{\text{eff}}$ and used below) is computed by dividing the quadrature conductivity by $\omega\varepsilon_0$ (refer to Eq. (21)).

**Table 2 Parameters of six cases with various clay types and salinities of pore water**

| Case | Clay types | Diameter of clay particles ($\mu$m) | Hydrate saturation | Hydrate distribution mode | Pore-water salinity (mol/L) |
|---|---|---|---|---|---|
| 1 | Kaolinite | 3.0 | 0.30 | fluid-suspending | $5\times10^{-4}$ and $5\times10^{-3}$ |
| 2 | Illite | | | | |
| 3 | Smectite | | | | |

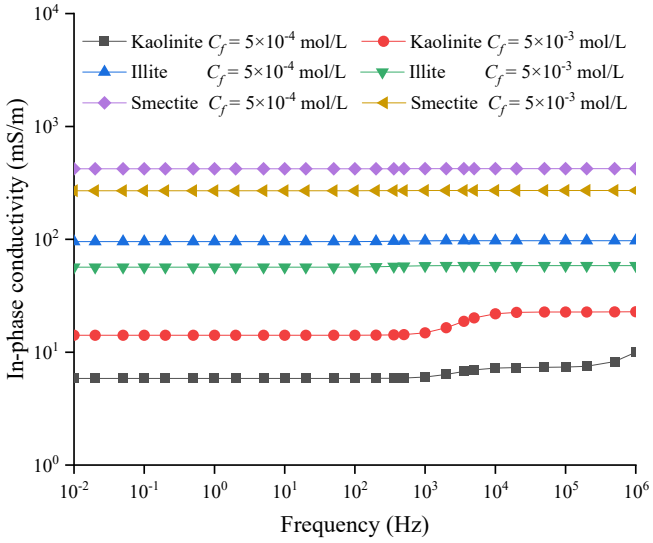
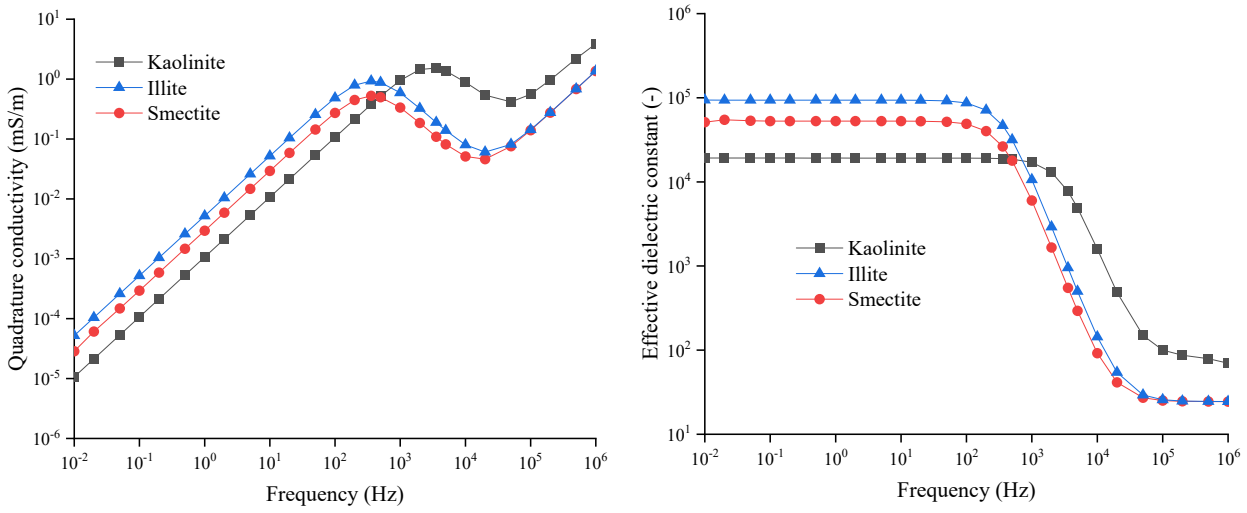



**Fig. 4 In-phase conductivity spectra of hydrate-bearing clays with different clay types and pore-water salinities**

As shown in **Fig. 4**, the in-phase conductivity of the hydrate-bearing kaolinite cases is the lowest, followed by the illite cases and the highest conductivity is obtained from the smectite cases. The in-phase conductivity of a medium essentially corresponds to the electrical conductance mechanism under an electric field. In the cases of hydrate-bearing sediments, the in-phase conductivity includes contributions from both the pore water and surface of clay particles (refer to Eq. (4)). This claim is applicable to the kaolinite cases but not to the smectite and illite cases as explained in **Section 2.3** and below. Due to the much higher specific surface areas of smectite and illite than that of kaolinite in reality, it is assumed that the pore space, left after the occupation of clay (i.e., smectite and illite) particles and hydrate clusters, has been filled with the diffuse layer of clay particles. This is reasonable under conditions of low pore-water salinities, e.g. lower than 0.01 mol/L (Leroy and Revil, 2009). For the smectite and illite cases, the in-phase conductivity of the REV is only attributed to the surface (in-phase)

conductivity in the diffuse layer of clay particles (i.e., ignoring the contribution of pore water). In the numerical models, the CEC of smectite, illite and kaolinite is assigned to be 1.0 C/kg, 0.3 C/kg and 0.09 C/kg, respectively (Jiang et al., 2018b). The surface conductivity due to the diffuse layer is proportional to the CEC (refer to Eqs. (6) and (7)) because the surface charge density in the diffuse layer relates to both the CEC and surface conductivity proportionally. Therefore, the in-phase conductivity of hydrate-bearing smectite is significantly higher than that of hydrate-bearing illite and kaolinite due to the large differences of CEC among the clay minerals.

It is interesting to observe different salinity effects on the hydrate-bearing smectite/illite and kaolinite in **Fig. 4**. For the kaolinite cases the in-phase conductivity increases with an increasing pore-water salinity from $5\times10^{-4}$ to $5\times10^{-3}$ mol/L, while an opposite trend appears in the smectite and illite cases. As mentioned above, for the smectite and illite cases, the pore-water conductivity does not contribute to the in-phase conductivity significantly but the surface conductivity induced by the diffuse layer does. Therefore, the salinity effects on the surface conductivity of the diffuse layer should be analyzed. As presented in **Section 2.3** the effective pore-water conductivity, i.e., the conductivity induced by the diffuse layer in essence, can be calculated with Eqs. (18) – (20) for hydrate-bearing smectite and illite cases. The required parameters include the mobility of counterions in the diffuse layer ($\beta_{(+)}$), CEC, partition coefficient ($f_{pc}$), mass density of grains ($\rho_s$), and porosity ($\varphi$). For a specific case with the clay mineral of smectite or illite, only the partition coefficient is affected by the pore-water salinity among those parameters (Arulanandan, 1969; Leroy et al., 2006). It has been reported by Leroy and Revil (2009) that the partition coefficient increases from 0.75 to 0.84 and from 0.82 to 0.89 for smectite and illite, respectively, with an increase of the pore-water salinity from $5\times10^{-4}$ to $5\times10^{-3}$ mol/L. An increase in the partition coefficient results in a reduction of the volumetric charge density ($\overline{Q}_V$) in the pore water (refer to Eq. (19)). As a result, for these specific cases of hydrate-bearing smectite and illite introduced above, the in-phase conductivity drops with an increasing salinity of the pore water.




(a) Quadrature conductivity (b) Effective dielectric constant

**Fig. 5 Spectra of the quadrature conductivity and effective dielectric constant of hydrate-bearing clays for cases with different types of clay minerals ($C_f$ = 1×10$^{-3}$ mol/L)**

The quadrature conductivity and effective dielectric constant of hydrate-bearing clays exhibit noteworthy characteristics for different types of clay minerals as shown in **Fig. 5**. Different peak frequencies, where the quadrature conductivity arrives at its maximum, can be observed in **Fig. 5(a)** for the three cases. The discrepancy of the three peak frequencies can be attributed to the differences of the mobility of the counterions in Stern layer (refer to Eqs. (13) and (14)) directly. In the numerical models, the mobility of counterions in Stern layers is 2.68 ×10$^{-8}$, 2.69×10$^{-9}$ and 2.69×10$^{-9}$ m$^2$s$^{-1}$V$^{-1}$ (at 4°C) for the kaolinite, illite and smectite particles (Leroy and Revil, 2009), respectively. A higher mobility of the counterions corresponds to a shorter characteristic relaxation time ($\tau_p$) and a higher peak frequency ($f_{peak}$); therefore, a higher peak frequency than those of the illite and smectite cases appears in the hydrate-bearing kaolinite case. As shown in **Fig. 5(a)**, the peak frequencies are 3.57 kHz, 0.36 kHz and 0.36 kHz for the hydrate-bearing kaolinite, illite and smectite cases, respectively.

The maximum quadrature conductivities of hydrate-bearing kaolinite, illite and smectite are different as indicated by **Fig. 5(a)**. In the perspective of the low-frequency polarization mechanism as presented in **Section 2.2 and 2.3**, it is believed that the quadrature conductivity of the REV results from the quadrature surface conductivity (i.e., due to the electrochemical polarization of EDL coating the solid particles). Additionally, by substituting $\omega\tau_p = 1$ into Eq. (10), we can obtain the expression $\sigma_s^{''} = \beta_{(+)}^{S} e\Gamma_{(+)}^{S0} / \Lambda$ for computing the

maximum quadrature surface conductivity. In the numerical models the surface site densities of the counterions ($\Gamma_{(+)}^{S0}$) are $0.450 \times 10^{-18}$, $1.120 \times 10^{-18}$ and $0.631 \times 10^{-18}$ counterions/m$^2$ for the kaolinite, illite and smectite particles, respectively, with the pore-water salinity of $1\times10^{-3}$ mol/L (Leroy and Revil, 2009). Both the illite and smectite particles have a slightly higher surface site density ($\Gamma_{(+)}^{S0}$) than the kaolinite, however, the mobility of counterions in the Stern layer ($\beta_{(+)}^{S}$) for the kaolinite is about ten times of that for the illite and smectite. The mobility of counterions in Stern layers is $2.68\times10^{-8}$, $2.69\times10^{-9}$ and $2.69\times10^{-9}$ m$^2$s$^{-1}$V$^{-1}$ (at 4°C) for the kaolinite, illite and smectite (Leroy and Revil, 2009), respectively. This explains why the hydrate-bearing kaolinite has the highest value for the maximum quadrature conductivity.

The Stern-layer polarization mechanism controls the frequency-dispersion behavior of the quadrature conductivity in the frequency band lower than $f_{peak}$. Compared with the quadrature conductivity, the effective dielectric constant characterizes the intensity of electrochemical polarization of Stern layer more clearly. As demonstrated in **Fig. 5(b)** the effective dielectric constant remains nearly unchanged in the lower frequency band, suggesting a persistent and steady polarization process of EDL. The hydrate-bearing illite has the highest effective dielectric constant, while the kaolinite case has the lowest at a specific frequency in the EDL-polarization dominating range. This indicates that a stronger polarization of Stern layer occurs in the hydrate-bearing illite case than that in the smectite and kaolinite cases. The different polarization intensities of the three cases can be obtained by computing the effective dielectric constant (denoted as $\kappa_{eff}^{s}$, dimensionless) from quadrature surface conductivity using Eq. (23) below, which can be derived from Eqs. (10), (13) and (21).

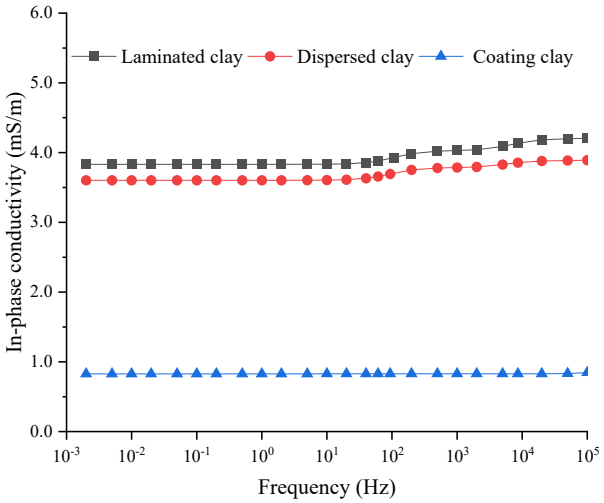
$$\kappa_{eff}^{s}=\frac{2\beta_{(+)}^{S}e\Gamma_{(+)}^{S0}\tau_p}{\Lambda\left(1+\omega^2\tau_p^2\right)\varepsilon_0} \tag{23}$$

### 4.3 Effects of clay distribution form

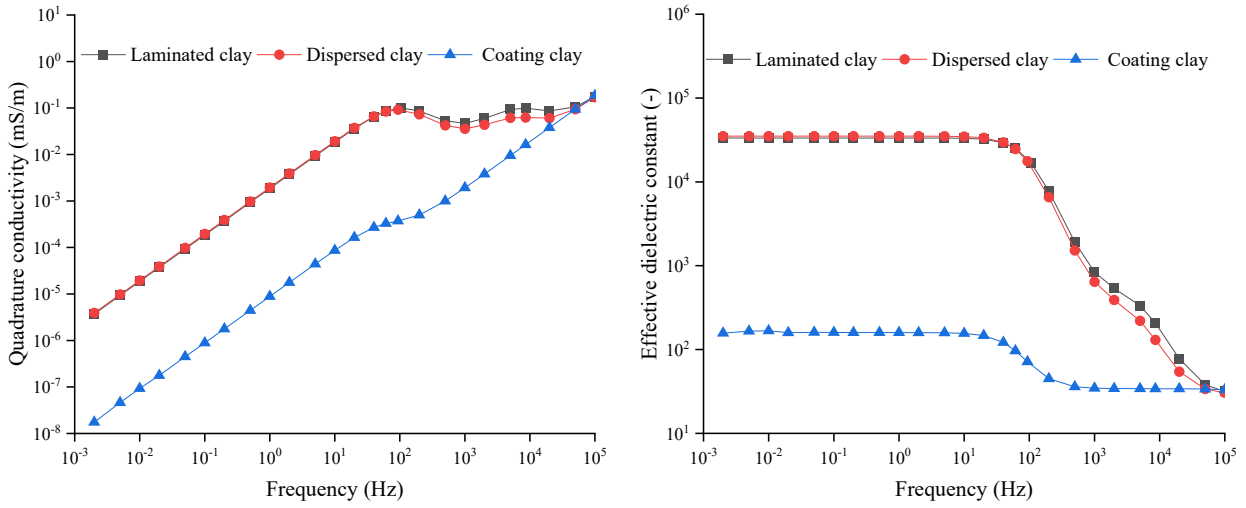
There are several typical distribution forms of clays in sediments as shown in **Fig. 1**. The clay distribution forms can be categorized into four classes, namely, dispersed clay, laminated clay, structural clay and coating clay (de Lima and Sharma 1990; Okay et al., 2014; Revil et al., 2015; Hu et al., 2019). To demonstrate the effects of clay distribution on complex conductivity, three typical distribution forms of kaolinite (as a representative of

the clay minerals concerned in this work) including dispersed, laminated and coating clays are modelled numerically. The same conditions such as the clay content, hydrate saturation, hydrate micro-distribution mode, porosity, and salinity are applied in the numerical models to achieve an appropriate and fair comparison of complex-conductivity responses among these cases. The structural clay is not included in this section but will be utilized for examining the effects of clay content and hydrate saturation in **Section 4.4 and 4.5**, respectively.

The frequency-dispersive spectra of in-phase/quadrature conductivities and effective dielectric constant for the three typical cases with laminated, dispersed and coating clays, respectively, are shown in **Fig. 6**. The clay content (6.0 % by volume), porosity ($\varphi$ = 0.34), pore-water salinity ($C_f = 1 \times 10^{-3}$ mol/L), hydrate saturation ($s_h$ = 0.20) and hydrate distribution mode (the suspending mode) remain the same for these cases. As demonstrated in **Fig. 6** similar complex-conductivity responses are obtained for hydrate-bearing clayey sands with laminated and dispersed clays, while the coating clay case exhibits remarkable discrepancies. The coating clay results in the lowest in-phase and quadrature conductivities, as well as the effective dielectric constant, consistently. Additionally, there are two peaks in the spectra of quadrature conductivity and effective dielectric constant for the laminated and dispersed clay cases. The peaks correspond to the two distinct characteristic relaxation times of EDL polarization, which results from the two diameters of sand and clay particles (i.e., 24 and 2.51 μm). The lower peak frequency around 100 Hz results from the larger particles, i.e., sand particles in the model.




(a) In-phase conductivity




(b) Quadrature conductivity (c) Effective dielectric constant

**Fig. 6 Spectra of the in-phase/quadrature conductivities and effective dielectric constant of hydrate-bearing kaolinite with different distribution forms of clays**

The pore-water conductance and surface conductance of solid particles (including sands and clays) are responsible for the in-phase conductivity of clayey sands containing hydrates (refer to **Fig. 6(a)**). For the three cases, the pore-water conductivity is exactly the same. Thus, the discrepancy of the in-phase conductivities among the three cases is attributed to the difference of surface in-phase conductivities of particles. According to the expression for the complex surface conductivity (i.e., Eq. (10)), the surface in-phase conductivity can be computed with Eq. (24) below.

$$\sigma_s'(\omega)=\sigma_s^{\infty}-\frac{\sigma_s^{\infty}-\sigma_s^{0}}{1+\omega^2\tau_p^2} \tag{24}$$

As the same type of clay (i.e., kaolinite) is adopted in the laminated and dispersed clay cases, there is no difference of $\sigma_s^0$ and $\sigma_s^{\infty}$ used in Eq. (24) between the two cases. Therefore, the characteristic relaxation time $\tau_p$ (refer to Eq. (13)) determines the relative amplitude relationship of the in-phase conductivity for the laminated and dispersed clay cases. For the laminated clay case, the characteristic relaxation time is $1.5\times10^{-3}$ and $1.6\times10^{-5}$ s, respectively, corresponding to the lower and higher peak frequencies. For the dispersed clay case, the characteristic relaxation time is $1.7\times10^{-3}$ and $1.9\times10^{-5}$ s, respectively. The difference of $\tau_p$ between the two cases results from the different cementation exponents and formation factors in Eqs. (13) and (14), which physically

reflects the different distribution forms of clay particles. As a result, the in-phase conductivity for the dispersed clay case is slightly lower than that for the laminated clay case. For the coating clay case, the sand particles have no contact with the pore water. As a result, no EDL can form on the surface of sand particles. Consequently, only the EDL coating the clay particles and the corresponding surface in-phase conductivity contributes to the in-phase conductivity of the REV. The surface in-phase conductivity of the clay-coating sand particles can be calculated with Eq. (25) below (de Lima and Sharma 1990).

$$\sigma_s^{'} = \frac{2\gamma\sigma_{sc}^{'}}{3-\gamma} \tag{25}$$

where $\sigma_{sc}^{'}$ is the surface in-phase conductivity of a clay particle (which can be calculated with Eq. (24)), and $\gamma$ is the clay volume fraction in a clay-coating particle (This is different from the term 'clay content', which is the ratio of the clay volume to the whole porous media). The surface in-phase conductivity for the laminated, dispersed and coating clay cases is 3.929, 3.693, and 0.828 mS/m, respectively, which explains the relative amplitude relationship of the in-phase conductivity for the three cases shown in **Fig. 6(a)**. A similar analysis on the quadrature conductivity as well as the effective dielectric constant can be made to explain the lowest amplitudes for the coating case, which is not presented here for brevity.

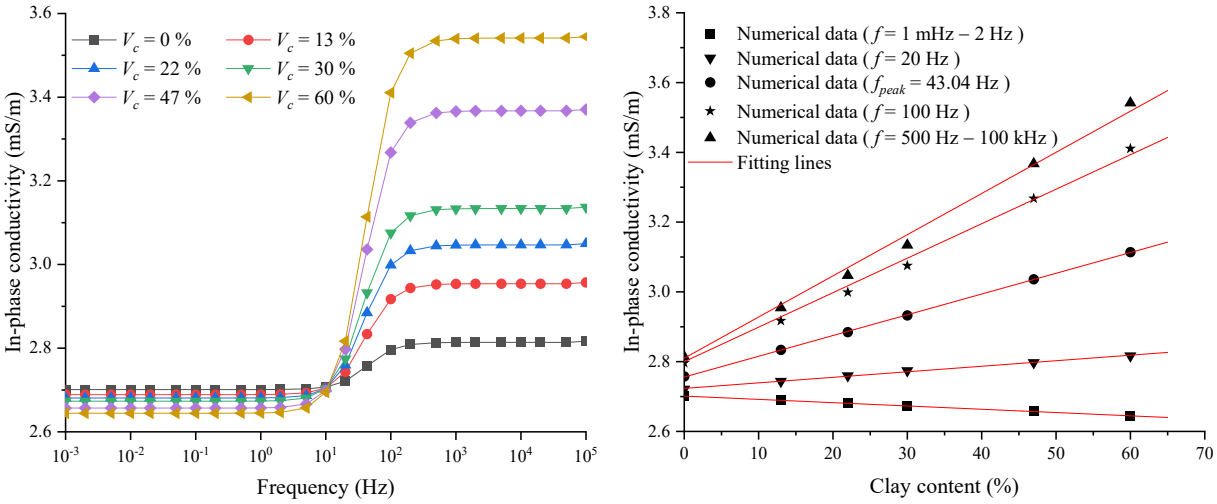
### 4.4 Effects of clay content

The effects of clay content (i.e., the volumetric fraction of clay in the porous material, denoted as $V_c$ below) on the complex conductivity of clayey sands containing hydrates are examined based on the numerical modelling scheme. The kaolinite of a structural distribution form is utilized as a representative of clay minerals and distribution forms. A range of clay contents from 0 to 60 % (by volume) are obtained by varying the count of sand particles replaced by kaolinite. In the numerical models, the hydrate saturation, porosity and pore-water salinity are 0.20, 0.40 and 0.001 mol/L, respectively.

The in-phase conductivity spectra for hydrate-bearing clayey sands with various clay contents are shown in **Fig. 7(a)**. The test frequency range can be split into lower and higher bands by the peak frequency. In the lower and higher frequency bands, it is clear that the clay content has different effects on the in-phase conductivity. The

in-phase conductivity increases with an increasing clay content in the higher frequency band. An opposite trend of clay effects on the in-phase conductivity can be observed in the lower frequency band. Similar to the analysis in the above sections, the differences of in-phase conductivity of the REV is attributed to the surface in-phase conductivity of particles, i.e., sand particles and clay particles for these specific cases in this section. After a computation of the surface in-phase conductivity using Eq. (24) for sand and kaolinite particles, it can be found that the surface in-phase conductivity of kaolinite is higher and lower than that of sand, respectively, in the higher and lower frequency bands. For example, the surface in-phase conductivities of kaolinite and sand particles with EDLs are 2.734 mS/m and 1.747 mS/m at 1 kHz (located in the higher frequency band), and 1.526 mS/m and 1.599 mS/m at 1 Hz (located in the lower frequency band), respectively. As introduced above, more sand particles are replaced by the kaolinite particles for a higher clay content. Therefore, the in-phase conductivity of the REV follows the same behavior with the surface in-phase conductivity of particles for an increasing clay content.

Typical frequencies are selected and the corresponding in-phase conductivities are plotted against the clay content in **Fig. 7(b)**. Nearly linear relationship between the clay content and in-phase conductivity can be identified. Therefore, the relationship between the clay content and in-phase conductivity is fitted with a linear model (i.e., $Y_\sigma = Y_{k\sigma} \times V_c + Y_{b\sigma}$) based on the least square principle. The intercept ($Y_{b\sigma}$) on the vertical axis of the plot represents exactly the in-phase conductivity of hydrate-bearing sands without clay. The slope ($Y_{k\sigma}$) obtained from the linear fitting operation and intercept ($Y_{b\sigma}$) are listed in **Table 3**. The linear correlations can be used as interpretation models for evaluating the clay contents in clayey sands with the measured in-phase conductivity.




(a) In-phase conductivity (b) In-phase conductivity against clay content

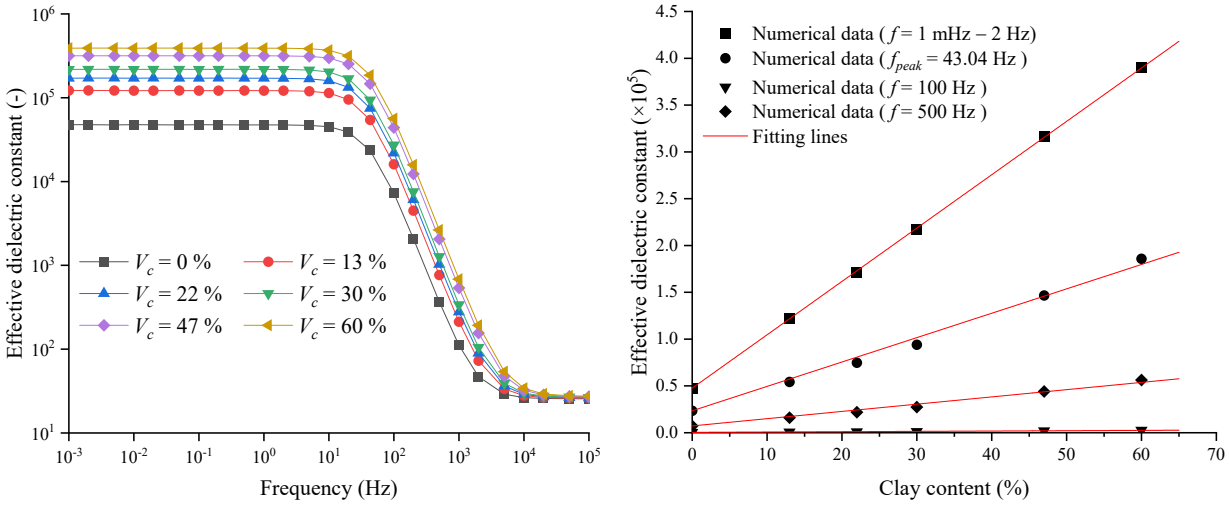
**Fig. 7 In-phase conductivity spectra of hydrate-bearing kaolinite and relation with the clay content**

**Table 3 Slope and intercept of fitting lines between the in-phase conductivity and clay content**

| Case | $f$ (Hz) | $Y_{k\sigma}$ (mS/m) | $Y_{b\sigma}$ (mS/m) |
|---|---|---|---|
| 1 | 0.001 – 2 | -0.094 | 2.70 |
| 2 | 20 | 0.159 | 2.72 |
| 3 | 43.04 ($f_{peak}$) | 0.595 | 2.76 |
| 4 | 100 | 0.989 | 2.80 |
| 5 | 500 – $10^5$ | 1.180 | 2.81 |

The variations of effective dielectric constant of hydrate-bearing clayey sands with frequency are shown in **Fig. 7(b)** for different clay contents. A consistent trend can be found that the effective dielectric constant at a specific frequency increases monotonically with an increasing clay content. This trend is reasonable because the clay mineral has a significantly higher CEC than that of sands, which results in a much higher quadrature surface conductivity for clay particles (refer to Eq. (16)). The relationship between the effective dielectric constant for the typical frequencies and clay content is then fitted with a linear model (i.e., $Y_{\kappa}=Y_{k\kappa}\times V_c+Y_{b\kappa}$) based on the least square principle. The intercept ($Y_{b\kappa}$) on the vertical axis of the plot is the effective dielectric constant of hydrate-bearing sands without clay. Both the slope ($Y_{k\kappa}$) obtained from the linear fitting operation and intercept ($Y_{b\kappa}$) are listed in **Table 4**. The linear correlations can also be used as models for evaluating the clay contents in clayey

sands with known effective dielectric constant.




(a) Effective dielectric constant (b) Effective dielectric constant against clay content

**Fig. 8 Spectra of the effective dielectric constant of hydrate-bearing kaolinite and relation with the clay content**

**Table 4 Slope and intercept of fitting lines between the effective dielectric constant and clay content**

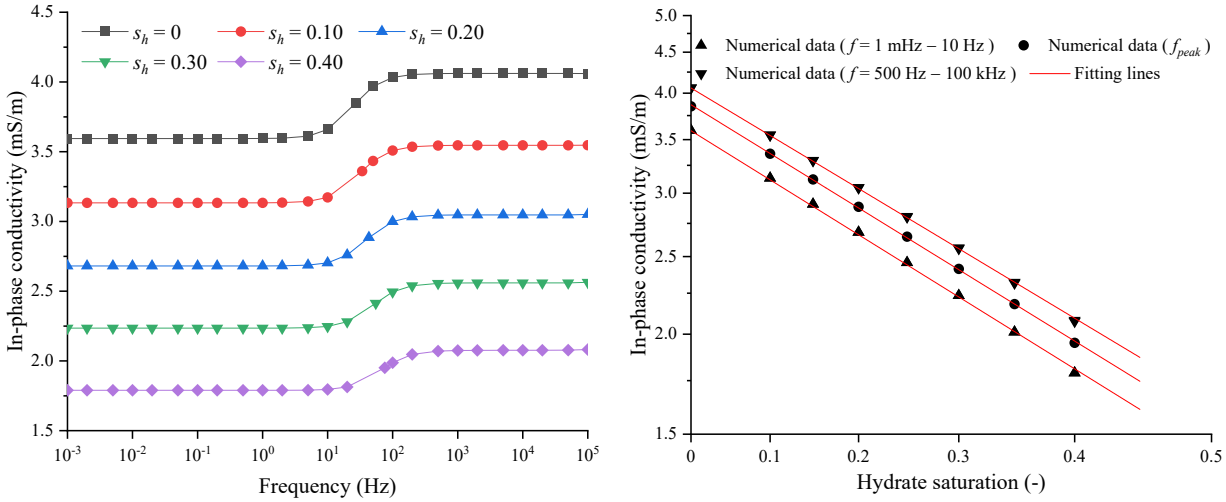
| Case | $f$ (Hz) | $Y_{k\kappa}$ (×10$^4$) | $Y_{b\kappa}$ (×10$^3$) |
|---|---|---|---|
| 1 | 0.001 – 2 | 57.0 | 47.6 |
| 2 | 43.04 ($f_{peak}$) | 26.0 | 23.5 |
| 3 | 100 | 7.75 | 7.28 |
| 4 | 500 | 0.36 | 0.37 |

## 4.5 Effects of hydrate saturation

The influences of hydrate saturation on the complex conductivity of clayey sands are examined with the numerical modelling method. The kaolinite of a structural distribution form is utilized as a representative of clay minerals and distribution forms in the models. A range of hydrate saturation from 0 to 0.40 are obtained by varying the diameter of circular surfaces representing hydrate clusters. In these numerical models, the clay content, porosity and pore-water salinity are 21.81 %, 0.40 and 0.001 mol/L, respectively.

The in-phase conductivity spectra of hydrate-bearing clayey sands with a variety of hydrate saturations are

presented in **Fig. 9(a)**. Generally, a clear trend can be identified that the in-phase conductivity decreases with an increasing hydrate saturation. It has been accepted that the conductivity of hydrate is very low and thus it can be considered as an insulator. The increased count of hydrate clusters in the pore space results in a shrinkage of the flow path for the current. As a result, the conductance of the REV decreases. The in-phase conductivity is then correlated with hydrate saturation using a power law expression with a reference to the Archie's model (Archie, 1942). Three typical frequencies, i.e., one in the lower frequency band (i.e., 0.001 – 10 Hz), the $f_{peak}$ and one in the higher frequency band (500 – $10^5$ Hz), are selected for establishing the correlations, respectively. The expression, i.e., $Y_{\sigma'} = Y_{0\sigma'}\left(1-s_h\right)^{n^*_{\sigma'}}$, is adopted and the parameters are fitted based on a least square principle. **Fig. 9(b)** and **Table 5** present the fitting lines and parameters for these fitted correlations.




(a) In-phase conductivity (b) In-phase conductivity against hydrate saturation

**Fig. 9 In-phase conductivity spectra of hydrate-bearing kaolinite with different hydrate saturations**

**Table 5 Parameters of correlations between the in-phase conductivity and hydrate saturation**

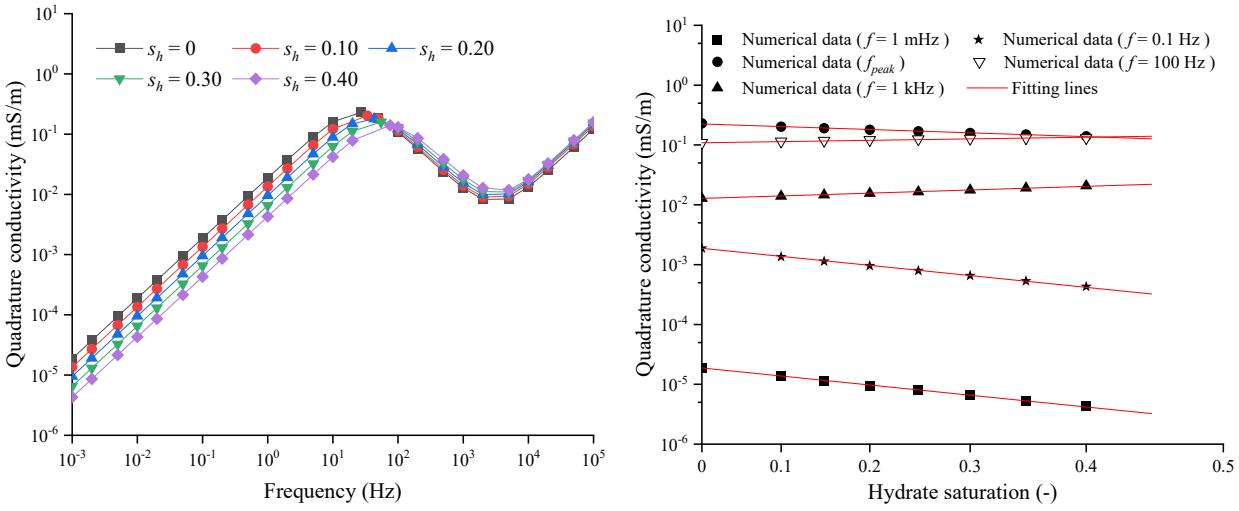
| Case | $f$ (Hz) | $Y_{0\sigma'}$ (mS/m) | $n^*_{\sigma'}$ |
|---|---|---|---|
| 1 | 0.001 – 10 | 3.59 | 1.30 |
| 2 | $f_{peak}$ | 3.90 | 1.33 |
| 3 | 500 – $10^5$ Hz | 4.06 | 1.34 |

The quadrature-conductivity spectra of clayey sands with various hydrate saturations are presented in **Fig. 10(a)**. It can be seen that the $f_{peak}$ increases (i.e., the characteristic relaxation time $\tau_p$ decreases) with an increasing

hydrate saturation ($s_h$). With a reference to Eq. (13) it can be understood that the reduction of $\tau_p$ results from a decrease of the water saturation ($s_w$=1–$s_h$). In the lower frequency band (i.e., 0.001 – 10 Hz) and at the peak frequencies, the quadrature conductivity decreases with hydrate saturation, while in the higher frequency band (i.e., 100 – 1000 Hz) an opposite trend can be found. It has been analyzed theoretically in **Section 2** that the EDL polarization process dominates in the lower frequency band (Revil, 2012; Niu et al., 2016, 2022). Therefore, the quadrature surface conductivity can be calculated with Eq. (26) for different hydrate saturations according to Eqs. (8), (9) and (10). It can be derived from Eq. (26) that an increased quadrature surface conductivity of particles is induced by an elevation of hydrate saturation with a correction factor of $\left(1-s_h\right)^p$ compared with that for saturated cases.

$$\sigma_s^{''}=\left(1-s_h\right)^p \frac{(\sigma_s^{\infty}-\sigma_s^{0})\omega\tau_p}{1+\omega^2\tau_p^2} \tag{26}$$

In the higher frequency band, the intensity of the EDL polarization and Maxwell-Wagner (MW) polarization decreases and increases with an increasing frequency, respectively. Therefore, a competition between the two polarization processes occurs, which results in a complex variation behavior of the quadrature conductivity with hydrate saturation. The quadrature conductivity is then correlated with hydrate saturation using a power law expression, which is similar to that for the in-phase conductivity. Five typical frequencies representing the lower frequency band, the critical frequency (i.e., the peak frequency) and the higher frequency band are used for establishing the correlations, respectively. The expression, i.e., $Y_{\sigma''}=Y_{0\sigma''}\left(1-s_h\right)^{n^*_{\sigma''}}$, is adopted and the parameters are fitted based on the least square principle. **Fig. 10(b)** and **Table 6** present the fitting lines and parameters for the fitted correlations.



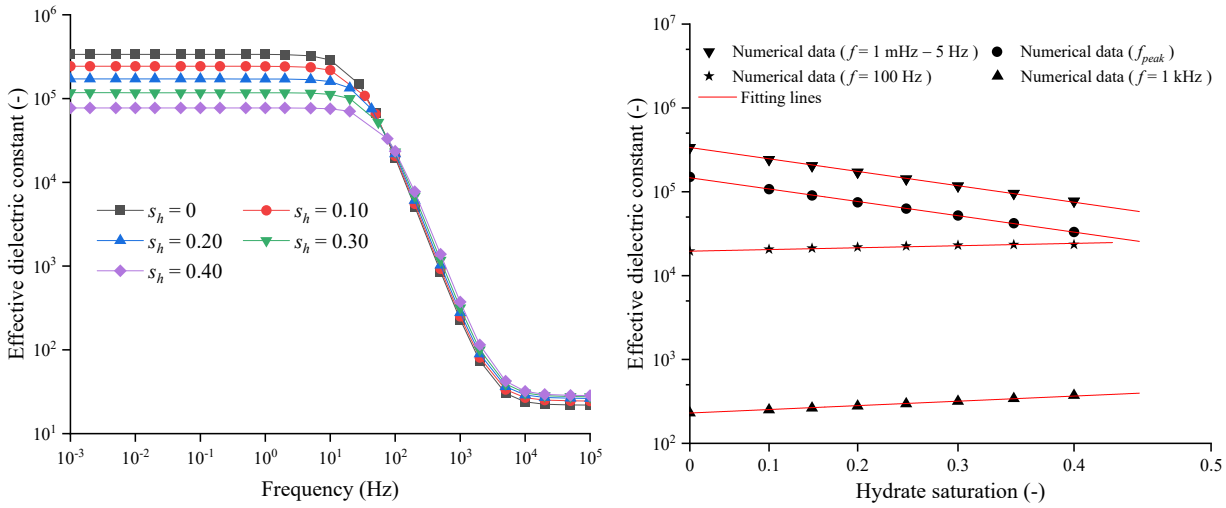

(a) Quadrature conductivity (b) Quadrature conductivity against hydrate saturation

**Fig. 10 Quadrature-conductivity spectra of hydrate-bearing kaolinite with different hydrate saturations**

**Table 6 Parameters of correlations between the quadrature conductivity and hydrate saturation**

| Case | $f$ (Hz) | $Y_{0\sigma''}$ (mS/m) | $n^*_{\sigma''}$ |
|---|---|---|---|
| 1 | 0.001 | $1.88\times10^{-5}$ | 2.94 |
| 2 | 0.1 | $1.88\times10^{-3}$ | 2.94 |
| 3 | $f_{peak}$ | $2.25\times10^{-1}$ | 0.96 |
| 4 | 100 | $1.09\times10^{-1}$ | -0.42 |
| 5 | 1000 | $1.09\times10^{-2}$ | -0.42 |

**Fig. 11(a)** demonstrates that the frequency-dispersive spectra of the effective dielectric constant of hydrate-bearing clayey sands vary with the hydrate saturation. It can be observed that the effective dielectric constant in the lower and higher frequency bands decreases and increases, respectively, with an increasing $s_h$. A power law expression is adopted to correlate the effective dielectric constant with hydrate saturation. Typical frequencies representing the lower frequency band, the critical frequency and the higher frequency band are used for establishing the correlations, respectively. The expression, i.e., $Y_\kappa = Y_{0\kappa}\left(1-s_h\right)^{n^*_\kappa}$, is adopted and the parameters are fitted based on the least square principle. The fitting lines and parameters for the fitted correlations are presented in **Fig. 11(b)** and **Table 7**. The correlations can be used as interpretation models for evaluating the hydrate saturation in clayey sands based on the measured complex conductivity.




(a) Effective dielectric constant (b) Effective dielectric constant against hydrate saturation

**Fig. 11 Effective-dielectric-constant spectra of hydrate-bearing kaolinite with various hydrate saturations**

**Table 7 Parameters of correlations between the effective dielectric constant and hydrate saturation**

| Case | $f$ (Hz) | $Y_{0\kappa}$ (×10⁴) | $n_{\kappa}^{*}$ |
|---|---|---|---|
| 1 | 0.001 – 5 | 33.7 | 2.94 |
| 2 | $f_{peak}$ | 14.7 | 2.92 |
| 3 | 100 | 1.96 | -0.42 |
| 4 | 1000 | 0.023 | -0.91 |

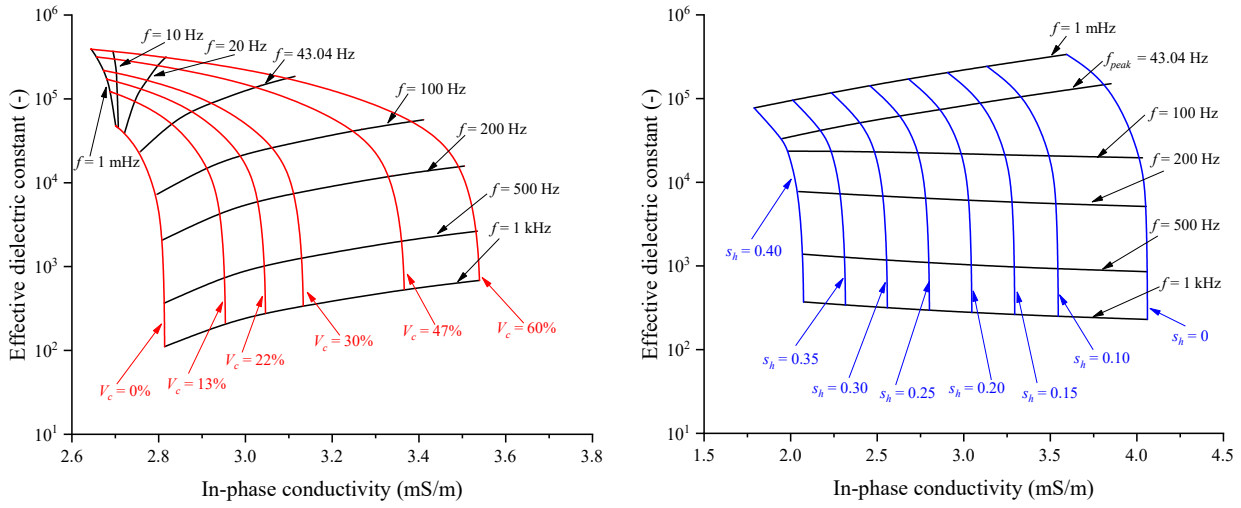
# 5 Discussion

## 5.1 Hydrate-reservoir evaluation based on joint conductance and polarization mechanisms

Borehole geophysical techniques are of significant importance to evaluating hydrate-reservoir parameters quantitatively. Due to the complexity nature of hydrate-bearing sediments and multiple solutions of well-logging interpretation, it is quite difficult to determine hydrate-reservoir parameters accurately by using the resistivity or dielectric constant alone. A joint interpretation of the conductivity and dielectric permittivity data is recommended to alleviate the severity of the multi-solution problem in data interpretation and reduce the uncertainty of the resultant reservoir parameters. Complex-conductivity measurements on hydrate-bearing

sands (clean sands without any clay) of various hydrate saturations have been collected over the frequency range from 20 Hz to 100 kHz by Xing et al. (2022). It has been shown that a fusion model incorporating the mechanisms of both the electrical conductance and electrochemical polarization of EDL performs the best for estimating the hydrate saturation than models based on the conductance or polarization mechanism alone.

In this work, the complex conductivity of hydrate-bearing clays and clayey sands have been analyzed in terms of frequency-dispersive spectra of the in-phase/quadrature conductivities and effective dielectric constant. To achieve a joint interpretation of the electrical responses controlled by the conduction and polarization mechanisms, cross-plots with the in-phase conductivity as the *x* axis and effective dielectric constant as the *y*-axis are constructed. **Fig. 12** shows the cross-plots for evaluating the clay content and hydrate saturation respectively. The frequency-dispersion characteristics of complex conductivity are also taken into consideration and demonstrated in the cross-plots.




(a) For clay content (b) For hydrate saturation

**Fig. 12 Cross-plots of in-phase conductivity and effective dielectric constant for resolving clay content and hydrate saturations**

## 5.2 Limitations of correlations for clay content and hydrate saturation

The clay content and hydrate saturation of hydrate-bearing clays and clayey sands have been correlated with

the complex-conductivity parameters, i.e., the in-phase conductivity, quadrature conductivity and effective dielectric constant, as presented in **Section 4.4 and 4.5**. Those correlations can be used as interpretation models for predicting the clay content and hydrate saturation when the complex-conductivity measurements are available. They will be very useful for interpreting the well-logging data in a wide frequency band (e.g., from ~ mHz to ~ kHz). However, there are some issues to be addressed further when extending the correlations established in this work to real applications.

Numerical models with the structural distribution form of clay as a representative have been constructed and solved in **Section 4.4 and 4.5**. As demonstrated **in Fig. 1** there are other three typical distribution forms of clays, i.e., the dispersed clay, laminated clay, and coating clay. It has also been demonstrated based on the numerical models in **Section 4.2** that the clay distribution form affects the complex-conductivity responses significantly, especially the coating clay. Despite of knowing the effects of clay distribution forms we had to select a representative distribution form (i.e., the structural clay) to achieve a fair and reasonable comparison among the numerical cases for reasons explained below.

To quantitatively evaluate the effects induced by different clay contents, the parameters such as hydrate saturation, porosity, formation factor, and cementation exponent have to be kept the same for the cases under comparison. Because all of these parameters affect the resultant complex-conductivity responses of the REVs. However, it is quite difficult (if not impossible) to meet this basic requirement for the distribution forms such as dispersed, laminated, and coating clays in the numerical models. Because the porosity as well as the related saturation and formation factor vary with the change of clay content for those distribution forms of clays. It can be anticipated that this problem is much more severe in experimental tests. To make sure that the porosity is unchanged the size of the sand particles has to be modified. Consequently, there would be different sized sand particles in the model geometries, resulting in different characteristic relaxation times as well as the complex-conductivity spectra of the REVs. Similar scenarios would be encountered in the investigation of hydrate saturation effects as presented in **Section 4.5**. To summarize, care should be taken when extending the correlations for predicting the clay content and hydrate saturation of hydrate-bearing clayey sands to distribution forms other than structural clay.

### 5.3 Simplification to model structures for hydrate-bearing sediments

The computational domains representing REVs of hydrate-bearing sediments are constructed following the finite-element modelling scheme presented in **Section 3.1**. **Fig. 1** shows four typical computational domains for numerical cases with different clay-distribution forms, which have been used extensively in this work. It can be seen that there are some obvious simplifications when simulating the real structures of hydrate-bearing sands by using those computational domains.

Firstly, the solid phases including sand/clay particles and hydrate clusters are modelled with circular surfaces of identical diameters in this work. This means that the effects of shape factors of the solid phases on the complex-conductivity responses have been ignored. This simplification alleviates the challenge to deal with complex schemes for computing the characteristic relaxation time (refer to Eq. (13)) and for upscaling the surface conductance to the conductivity of the sand/clay particles (refer to Eqs. (10) and (17)). It has been reported that, if a statistical distribution of the particle diameters (e.g., Gaussian distribution, Cole-Cole distribution, etc.), it will be difficult to identify the peak frequency in the frequency-dispersive spectrum of quadrature conductivity (Lesmes and Frye, 2001; Revil et al., 2015). The subsection of the quadrature-conductivity spectrum showing a peak value for cases with the sand/clay particles of an identical diameter will be substituted by a section of spectrum characterized by multiple peaks or even a plateau.

Secondly, in this work, only the pore-filling mode of hydrates in clayey sands are taken into account in the numerical cases. The extension of the results from cases with the pore-filling mode of hydrates in clayey sands to other cases with the particle-displacive and particle-wrapped segregated hydrate morphologies in clayey-silty sediments (Wu et al., 2022) could be invalid. It has been reported that gas hydrates may exhibit a variety of micro-scale distribution modes in porous materials based on a series of experimental observations for $CH_4$ hydrates or $CO_2$ hydrates (Kerkar et al., 2009; Dai et al., 2012; Ta et al., 2015; Yang et al., 2015; Lei et al., 2019; Kou et al., 2021; Li et al., 2022; Wu et al., 2022). It is reported that the hydrate in clayey-silty sediments mainly presents patchy distribution form. At the pore scale, it could be particle-displacive and particle-wrapped segregated hydrate morphology, which is different from those in sandy sediments (Wu et al., 2022). The physical properties (e.g.,

electrical, acoustic, thermal, mechanical, hydraulic, etc.) of sediments are highly affected by the micro-distribution modes of hydrates. In the perspective of electrical properties, the micro-distribution mode of hydrate has been classified into two classes, i.e. the fluid-suspending mode (or called the pore-filling mode) and the grain-attaching mode (including the grain-coating and grain-cementing modes), as demonstrated in Xing et al. (2021). The hydrate does not contact with the surfaces of particles, e.g., sand or clay, for the pore-filling mode. We have noted that the surface area of sand/clay particles coated by hydrate varies in a large range even at the same hydrate saturation. It can be envisaged that the contact interface between the hydrate and particles could disturb the original state of EDL and the disturbance could result in significant impacts on the in-phase/quadrature conductivities of the REV. However, there are still open questions, e.g., how the EDL is disturbed, and how the influences of the disturbance on complex conductivity is quantified. The questions need to be answered properly before managing to build reliable models relating the complex-conductivity parameters to hydrate saturation.

Thirdly, the model structures used in the numerical scheme of this work are mainly applicable to unconsolidated sediments, and some issues need to be noted before using them for modelling consolidated sediments. It is widely accepted that natural gas hydrates also exist in terrestrial permafrost areas. The lithology of hydrate reservoirs in permafrost areas is dominated by dense rock types such as mudstone, siltstone and fine sandstone (Dong et al., 2019; Hu et al., 2019), which are characterized by low porosity and low hydrate saturation. As a comparison, the unconsolidated marine sediments containing hydrates usually have much higher porosity and relatively higher saturation. In this work, we constructed 2D computational domains to represent the model structures characterized by high porosities corresponding to unconsolidated marine sediments. Both the electrical conduction and polarization mechanisms can be resolved appropriately as demonstrated in detail by Xing et al. (2021) and this work. However, challenges may arise when using the 2D model structures for simulating low-porosity consolidated sediments due to the narrow paths with a high tortuosity for the electrical current to flow. For those tight stones, 3D models are recommended because the complex conduction paths can be simulated in a more reasonable way (Dong et al., 2018). It needs to be mentioned that the complexity of the 3D models for hydrate-bearing clayey sediments is higher than that of 2D models by far in terms of the spatial arrangement of sand/clay/hydrate particles or clusters. The same issues discussed in the second and third

paragraphs in **Section 5.3** also arise if considering the stress-induced particle deformation and the disturbed EDLs coating the packing sand/clay particles. It deserves dedicated work to establish 3D numerical models for hydrate-bearing unconsolidated/consolidated sediments and investigate the complex-conductivity responses systematically.

# 6 Conclusions

To investigate the influences of clay minerals on low-frequency complex-conductivity responses of sediments containing hydrates, a pore-scale numerical study has been carried out based on finite-element (FE) numerical models. The effects of clay type, clay distribution form, clay content, and hydrate saturation on the spectra of complex conductivity have been analyzed systematically. Correlations have been derived for evaluating the clay content and hydrate saturation from complex-conductivity parameters. The following conclusions are derived from this work.

(1) The electrical properties of clayey sands containing hydrates can be characterized thoroughly by the frequency-dispersive spectra of complex conductivity. The low-frequency complex conductivity can be modelled numerically based on the mechanisms of electrical conduction and electrochemical polarization of EDLs. An interpretation of the complex-conductivity parameters obtained from the FE models provides micro-scale understandings of the clay effects on the low-frequency electrical properties of sediments.

(2) The in-phase conductivity of hydrate-bearing smectite is higher than that of hydrate-bearing illite and kaolinite in response to the higher CEC of smectite. Higher peak frequency and quadrature conductivity appear for the hydrate-bearing kaolinite case because the mobility of counterions in the Stern layer of kaolinite is about ten times of that for smectite and illite. The in-phase and quadrature conductivities for the coating-clay case are lower than the dispersed and laminated clay cases, because the coating clay isolates sands from the pore water and thus no EDL can form around the sand particles.

(3) With an increasing content of the structural clay up to 60 %, the in-phase conductivity decreases and increases in the frequency bands lower and higher, respectively, than the peak frequency corresponding to the EDL polarization. The effective dielectric constant increases consistently with the clay content due to the much higher CEC of clays than that of sands. Linear correlations can be established for evaluating the

clay content based on the in-phase conductivity and effective dielectric constant, respectively.

(4) The in-phase conductivity decreases consistently with an increasing hydrate saturation up to 0.40 due to the negligible conductivity of hydrates and blockage effect on conduction currents. Both the quadrature conductivity and effective dielectric constant in the EDL-polarization-dominant frequency band decrease with an increasing saturation of the fluid-suspending hydrate. Power-law correlations can be established for evaluating the hydrate saturation based on the complex-conductivity parameters.

The in-phase conductivity characterizes the electrical conduction process in hydrate-bearing clays and clayey sands quantitatively, while the quadrature conductivity and effective dielectric constant characterize the electrical polarization process. This suggests that the complex conductivity can be employed to capture the electrical characteristics of hydrate-bearing clayey sediments thoroughly. A great potential to quantitatively evaluate the clay content and hydrate saturation with a string of complex-conductivity parameters has been demonstrated in this study, which provides a theoretical and modelling foundation for the development of borehole IP-based geophysical techniques for hydrate-reservoir evaluation and monitoring in both the exploration and exploitation stages. The counterpart experimental tests on both artificial and field-retrieved samples of hydrate-bearing clayey sediments are planned for the future work.

## Nomenclature

***Symbols***

| | | | |
|---|---|---|---|
| $\mathbf{E}$ | Electrical field intensity, V/m | $\Gamma_{(+)}^{d}$ | Surface site density of counterions in diffuse layer, counterions/m$^2$ |
| $\mathbf{E_0}$ | Magnitude of electrical field intensity, V/m | $\Lambda$ | Characteristic pore/throat size, m |
| $\mathbf{J}$ | Total electric current density, A/m$^2$ | $\lvert q_{(+)}\rvert$ | Absolute value of the charge of counterions in Stern layer, C |
| $\mathbf{J_c}$ | Conduction current density, A/m$^2$ | $c$ | Cole-Cole exponent, dimensionless |

| | | | |
|---|---|---|---|
| $\mathbf{J_d}$ | Displacement current density, A/m$^2$ | $C_f$ | Salinity of pore water, mol/L |
| $V$ | Electric potential, V | $d$ | Grain diameter, m |
| $\varepsilon$ | Dielectric permittivity, F/m | $D_{(+)}^{S}$ | Diffusing coefficient of counterions in Stern layer, m$^2$/s |
| $\varepsilon_0$ | Dielectric permittivity in vacuum, $8.854\times10^{-12}$ F/m | $e$ | Elementary charge, $1.602\times10^{-19}$ C |
| $\varepsilon_{eff}$ | Effective permittivity, F/m | $f$ | Frequency, Hz |
| $\varepsilon'$ | Real part of $\varepsilon$, F/m | $f_{pc}$ | Partition coefficient, i.e., the relative count fraction of counterions in Stern layer to the whole electrical double layer, dimensionless |
| $\varepsilon''$ | Imaginary part of $\varepsilon$, F/m | $f_{peak}$ | Peak frequency, Hz |
| $\sigma$ | Electrical conductivity, S/m | $F$ | Intrinsic formation factor, dimensionless |
| $\sigma^*$ | Complex conductivity, S/m | $\sigma'$ | Real part of $\sigma^*$, i.e., in-phase conductivity, S/m |
| $\Gamma_{(+)}^{S0}$ | Surface site density of counterions in Stern layer, counterions/m$^2$ | $\sigma''$ | Imaginary part of $\sigma^*$, i.e., quadrature conductivity, S/m |
| $\alpha_w$ | Tortuosity of electromigration pathways along the surface of grains in water phase, dimensionless | $\sigma_{eff}^*$ | Effective complex conductivity, S/m |
| $\omega$ | Angular frequency, rad/s | $\sigma_{eff}$ | Effective conductivity, S/m |
| $\varphi$ | Connected porosity, dimensionless | $p$ | Saturation exponent for quadrature conductivity, dimensionless |
| $\tau_p$ | Characteristic relaxation time, s | $Q_d$ | Surface charge density in diffuse layer, C/m$^2$ |
| $\rho_s$ | Mass density of grains, kg/m$^3$ | $Q_s$ | Mean charge density for solid phase, C/m$^2$ |
| $\sigma_s'$ | In-phase conductivity of surface conductivity, S/m | $\overline{Q}_V$ | Volumetric charge density in pore water, C/m$^3$ |

| | | | |
|---|---|---|---|
| $\sigma_s''$ | Quadrature conductivity of surface conductivity, S/m | $Q_V$ | Total bulk charge density, C/m$^3$ |
| $\sigma_s^0$ | Low-frequency (in-phase) conductivity of solid phase, S/m | $s_h$ | Hydrate saturation, dimensionless |
| $\sigma_s^\infty$ | High-frequency (in-phase) conductivity of solid phase, S/m | $s_w$ | Water saturation, dimensionless |
| $\sigma^0$ | Low-frequency electrical conductivity, S/m | $S$ | Surface area of solid grains, m$^2$ |
| $\sigma^\infty$ | High-frequency electrical conductivity, S/m | $S_{sp}$ | Specific surface area, m$^2$/kg |
| $\sigma_w$ | Pore-water conductivity, S/m | $T$ | Temperature, K |
| $\bar{\sigma}_w$ | Effective pore-water conductivity, S/m | $\sum_s^\infty$ | Specific surface conductivity from the contribution of Stern layer, S |
| $\sum_s^0$ | DC specific surface conductivity, i.e., specific surface conductivity from the contribution of diffuse layer, S | $\beta_{(+)}$ | Mobility of counterions in diffuse layer, m$^2$/(sv) |
| $\sigma_s^*$ | Complex surface conductivity, S/m | $\beta_{(+)}^\delta$ | Mobility of counterions in Stern layer, m$^2$/(sv) |
| $K_b$ | Boltzmann constant, J/K | $V_c$ | Clay content, % |
| $\kappa_{eff}$ | Effective dielectric constant, dimensionless | $V_s$ | Volume of the grains, m$^3$ |
| $m$ | Cementation exponent, dimensionless | $\gamma$ | Clay volume fraction in a clay-coating particle, dimensionless |
| $n$ | Saturation exponent, dimensionless | | |

***Abbreviation***

| | | | |
|---|---|---|---|
| CEC | Cation exchange capacity | FE | Finite element |
| DEM | Differential effective medium | HBS | Hydrate-bearing sediment |

| | | | |
|---|---|---|---|
| EDL | Electrical double layer | REV | Representative elementary volume |
| EMT | Effective medium theory | SSA | Specific surface area |

## Acknowledgement

This work was supported by the Fundamental Research Funds for the Central Universities (20CX05005A), the Major Scientific and Technological Projects of CNPC (ZD2019-184-001), PetroChina Innovation Foundation (2018D-5007-0214), Shandong Provincial Natural Science Foundation (ZR2019MEE095) and National Natural Science Foundation of China (42174141). We are sincerely grateful to the editors and anonymous referees for their constructive comments.

## References

Archie, G. E., 1942. The electrical resistivity log as an aid in determining some reservoir characteristics, *Transactions of the AIME*, 146(1), 54–62.

Arulanandan, K., 1969. Hydraulic and electrical flows in clays, *Clays and Clay Minerals*, 17(2), 63–76.

Boswell, R., 2009. Is gas hydrate energy within reach?, *Science*, 325(5943), 957–958.

Boswell, R., Collett, T. S., 2011. Current perspectives on gas hydrate resources, *Energy & Environmental Science*, 4(4), 1206–1215.

Boswell, R., Hancock, S., Yamamoto, K., Collett, T., Pratap, M., Lee, S.R., 2020. Natural gas hydrates: status of potential as an energy resource. *Future Energy* 111–131.

Chibura, P. E., Zhang, W., Luo, A., Wang, J., 2022. A review on gas hydrate production feasibility for permafrost and marine hydrates. *Journal of Natural Gas Science and Engineering*, 100, 104441.

Chong, Z. R., Yang, S. H. B., Babu, P., Linga, P., Li, X. S., 2016. Review of natural gas hydrates as an energy resource: Prospects and challenges, *Applied Energy*, 162, 1633–1652.

Collett, T. S., 2002. Energy resource potential of natural gas hydrates, *AAPG Bulletin*, 86(11), 1971–1992.

Collett, T. S., Ladd, J., 2000. Detection of gas hydrates with downhole logs and assessment of gas hydrate concentrations (saturations) and gas volumes on the Blake Ridge with electrical resistivity log data, In

*Proceedings of the Ocean Drilling Program, Scientific Results*, 164, 179–191.

Cook, A. E., Waite, W. F., 2018. Archie's saturation exponent for natural gas hydrate in coarse-grained reservoirs, *Journal of Geophysical Research: Solid Earth*, 123, 2069–2089.

Dai, S., Lee, C., Santamarina, J. C., 2011. Formation history and physical properties of sediments from the Mount Elbert gas hydrate stratigraphic test well, Alaska North Slope, *Marine and Petroleum Geology*, 28(2), 427–438.

Dai, S., Santamarina, J. C., Waite, W. F., Kneafsey, T. J., 2012. Hydrate morphology: Physical properties of sands with patchy hydrate saturation, *Journal of Geophysical Research: Solid Earth*, 117(B11), 1–12.

de Lima, O. A., Sharma, M. M., 1990. A grain conductivity approach to shaly sandstones, *Geophysics*, 55(10), 1347–1356.

Dong, H., Sun, J., Cui, L., Naser, G., Yan, W., 2019. Characteristics of the pore structure of natural gas hydrate reservoir in the Qilian Mountain Permafrost, Northwest China, *Journal of Applied Geophysics*, 164, 153–159.

Dong, H., Sun, J., Lin, Z., Fang, H., Li, Y., et al., 2018. 3D pore-type digital rock modeling of natural gas hydrate for permafrost and numerical simulation of electrical properties, *Journal of Geophysics and Engineering*, 15, 275–285.

Dong, H., Sun, J., Zhu, J., Liu, L., Lin, Z., et al., 2019. Developing a new hydrate saturation calculation model for hydrate-bearing sediments, *Fuel*, 248, 27–37.

du Frane, W. L., Stern, L. A., Weitemeyer, K. A., Constable, S., Pinkston, J. C., et al., 2011. Electrical properties of polycrystalline methane hydrate, *Geophysical Research Letters*, 38(9), 1–5.

Freedman, R., Vogiatzis, J. P., 1986. Theory of induced-polarization logging in a borehole, *Geophysics*, 51(9), 1830–1849.

Han, H., Wang, Y., Li, X. S., Yu, J. X., Feng, J. C., et al., 2016. Experimental study on sediment deformation during methane hydrate decomposition in sandy and silty clay sediments with a novel experimental apparatus, *Fuel*, 182, 446–453.

Haukalid, K., Folgerø, K., Barth, T., Fjermestad, S. L., 2017. Hydrate formation in water-in-crude oil emulsions studied by broad-band permittivity measurements, *Energy & Fuels*, 31(4), 3793–3803.

Hu, X., Zou, C., Lu, Z., Yu, C., Peng, C., et al., 2019. Evaluation of gas hydrate saturation by effective medium

theory in shaly sands: a case study from the Qilian Mountain permafrost, China, *Journal of Geophysics and Engineering*, 16(1), 215–228.

Hu, C., Jia, Y., Duan, Z., 2022. Pore scale study of the permeability anisotropy of sands containing grain-coating and pore-filling hydrates, *Journal of Petroleum Science and Engineering*, 215, 110590.

Hyndman, R. D., Yuan, T., Moran, K., 1999. The concentration of deep sea gas hydrates from downhole electrical resistivity logs and laboratory data, *Earth and Planetary Science Letters*, 172(1–2), 167–177.

Jang, J., Santamarina, J. C., 2016. Hydrate bearing clayey sediments: Formation and gas production concepts, *Marine and Petroleum Geology*, 77, 235–246.

Jiang, M., Ke, S., Kang, Z., 2018a. Measurements of complex resistivity spectrum for formation evaluation, *Measurement*, 124, 359–366.

Jiang, S., Liang, P., Han, Y., 2018b. Effect of clay mineral composition on low-salinity water flooding, *Energies*, 11(12), 3317.

Jin, Y., Li, S., Yang, D., 2020. Experimental and theoretical quantification of the relationship between electrical resistivity and hydrate saturation in porous media, *Fuel*, 269, 117378.

Kerkar, P., Jones, K. W., Kleinberg, R., Lindquist, W. B., Tomov, S., et al., 2009. Direct observations of three dimensional growth of hydrates hosted in porous media, *Applied Physics Letters*, 95(2), 1–3.

Kim, H., Zheng, J., Yin, Z., Kumar, S., Tee, J., et al., 2022. An electrical resistivity-based method for measuring semi-clathrate hydrate formation kinetics: Application for cold storage and transport, *Applied Energy*, 308, 118397.

Koh, C. A., Sum, A. K. E., Sloan, E. D., 2012. State of the art: Natural gas hydrates as a natural resource, *Journal of Natural Gas Science and Engineering*, 8, 132–138.

Kou, X., Li, X., Wang, Y., Liu, J., Chen, Z., 2021. Effects of gas occurrence pattern on distribution and morphology characteristics of gas hydrates in porous media, *Energy*, 226, 120401.

Kumar, A., Sakpal, T., Roy, S., Kumar, R., 2015. Methane hydrate formation in a test sediment of sand and clay at various levels of water saturation, *Canadian Journal of Chemistry*, 93(8), 874–881.

Lee, J. Y., Francisca, F. M., Santamarina, J. C., Ruppel, C., 2010a. Parametric study of the physical properties of hydrate-bearing sand, silt, and clay sediments: 2. Small-strain mechanical properties, *Journal of Geophysical Research: Solid Earth*, 115, B11105.

Lee, J. Y., Santamarina, J. C., Ruppel, C., 2010b. Parametric study of the physical properties of hydrate-bearing sand, silt, and clay sediments: 1. electromagnetic properties, *Journal of Geophysical Research: Solid Earth*, 115, B11104.

Lee, M. W., 2011. Connectivity equation and shaly-sand correction for electrical resistivity, U.S. Geological Survey, Scientific Investigation Report 2011–5005, p. 9.

Lee, M. W., Collett, T. S., 2006. A method of shaly sand correction for estimating gas hydrate saturations using downhole electrical resistivity log data, U.S. Geological Survey, Scientific Investigation Report 2006–5121, p. 10.

Lee, M.W., Collett, T.S., 2009. Gas hydrate saturations estimated from fractured reservoir at Site NGHP-01-10, Krishna-Godavari Basin, India, *Journal of Geophysical Research: Solid Earth*, 114(B7), 261–281.

Lee, M. W., Collett, T. S., 2011. In-situ gas hydrate saturation estimated from various well logs at the Mount Elbert Gas Hydrate Stratigraphic Test Well, Alaska North Slope, *Marine and Petroleum Geology*, 28(2), 439–449.

Lei, L., Seol, Y., Choi, J. H., Kneafsey, T. J., 2019. Pore habit of methane hydrate and its evolution in sediment matrix–Laboratory visualization with phase-contrast micro-CT, *Marine and Petroleum Geology*, 104, 451–467.

Leroy, P., Revil, A., 2009. A mechanistic model for the spectral induced polarization of clay materials, *Journal of Geophysical Research: Solid Earth*, 114, B10202.

Leroy, P., Revil, A., Coelho, D., 2006. Diffusion of ionic species in bentonite, *Journal of Colloid & Interface Science*, 296(1), 248–255.

Leroy, P., Revil, A., Kemna, A., Cosenza, P., Ghorbani, A., 2008. Complex conductivity of water-saturated packs of glass beads, *Journal of Colloid and Interface Science*, 321(1), 103–117.

Lesmes, D. P., Frye, K. M., 2001. Influence of pore fluid chemistry on the complex conductivity and induced polarization responses of Berea sandstone, *Journal of Geophysical Research: Solid Earth*, 106(B3), 4079–4090.

Li, J., Ke, S., Yin, C., Kang, Z., Jia, J., et al., 2019. A laboratory study of complex resistivity spectra for predictions of reservoir properties in clear sands and shaly sands, *Journal of Petroleum Science and Engineering*, 177, 983–994.

Li, X., Wang, C., Li, Q., Pang, W., Chen, G., et al., 2022. Experimental observation of formation and dissociation of methane hydrate in a micromodel, *Chemical Engineering Science*, 248, 117227.

Liu, C., Ye, Y., Meng, Q., He, X., Lu, H., et al., 2012. The characteristics of gas hydrates recovered from Shenhu Area in the South China Sea, *Marine Geology*, 307, 22–27.

Liu, J., Li, X., 2021. Recent advances on natural gas hydrate exploration and development in the South China Sea, *Energy & Fuels*, 35(9), 7528–7552.

Liu, Z., Kim, J., Lei, L., Ning, F., Dai, S., 2019. Tetrahydrofuran hydrate in clayey sediments—laboratory formation, morphology, and wave characterization, *Journal of Geophysical Research: Solid Earth*, 124(4), 3307–3319.

Ma, X., Sun, Y., Guo, W., Jia, R., Li, B., 2020. Effects of irreducible fluid saturation and gas entry pressure on gas production from hydrate-bearing clayey silt sediments by depressurization. *Geofluids*, 2020(4), 1–20.

Mao, P., Wan, Y., Sun, J., Li, Y., Hu, G., et al., 2021. Numerical study of gas production from fine-grained hydrate reservoirs using a multilateral horizontal well system, *Applied Energy*, 301, 117450.

Milkov, A. V., 2004. Global estimates of hydrate-bound gas in marine sediments: how much is really out there?, *Earth-Science Reviews*, 66(3–4), 183–197.

Miyairi, M., Akihisa, K., Uchida, T., Collett, T. S., Dallimore, S. R., 1999. Well-log interpretation of gas-hydrate-bearing formations in the JAPEX/JNOC/GSC Mallik 2L-38 gas hydrate research well, *Bulletin of the Geological Survey of Canada*, 281–293.

Moridis, G. J., Collett, T. S., Boswell, R., Kurihara, M., Reagan, M. T., et al., 2009. Toward production from gas hydrates: current status, assessment of resources, and simulation-based evaluation of technology and potential, *SPE Reservoir Evaluation & Engineering*, 12(5), 745–771.

Ning, F., Wu N., Yu, Y., Zhang K., Jiang, G., et al., 2013a. Invasion of drilling mud into gas-hydrate-bearing sediments. Part II: effects of geophysical properties of sediments, *Geophysical Journal International*, 193(3), 1385–1398.

Ning, F., Zhang K., Wu N., Zhang, L., Li, G., et al., 2013b. Invasion of drilling mud into gas-hydrate-bearing sediments. Part I: effect of drilling mud properties, *Geophysical Journal International*, 193(3), 1370–1384.

Niu, Q., Prasad, M., Revil, A., Saidian, M., 2016. Textural control on the quadrature conductivity of porous media, *Geophysics*, 81(5), E297–E309.

Niu, Q., Zhang, C., 2017. Pore-scale modelling of complex conductivity of saturated granular materials, *Near Surface Geophysics*, 15(6), 593–602.

Niu, Q., Zhang, C., Prasad, M., 2020. A framework for pore-scale simulation of effective electrical conductivity and permittivity of porous media in the frequency range from 1 mHz to 1 GHz, *Journal of Geophysical Research: Solid Earth*, 125, e2020JB020515.

Okay, G., Leroy, P., Ghorbani, A., Cosenza, P., Camerlynck, C., et al., 2014. Spectral induced polarization of clay-sand mixtures: Experiments and modeling, *Geophysics*, 79(6), E353–E375.

Osterman, G., Keating, K., Binley, A., Slater, L., 2016. A laboratory study to estimate pore geometric parameters of sandstones using complex conductivity and nuclear magnetic resonance for permeability prediction, *Water Resources Research*, 52(6), 4321–4337.

Park, S. Y., Son, B. K., Choi J., Jin, H., Lee, K., 2022. Application of machine learning to quantification of mineral composition on gas hydrate-bearing sediments, Ulleung Basin, Korea, *Journal of Petroleum Science and Engineering*, 209, 109840.

Ren, J., Liu, X., Niu, M., Yin, Z., 2022. Effect of sodium montmorillonite clay on the kinetics of $CH_4$ hydrate-implication for energy recovery, *Chemical Engineering Journal*, 437, 135368.

Revil, A., 2012. Spectral induced polarization of shaly sands: Influence of the electrical double layer, *Water Resources Research*, 48(2), 1–23.

Revil, A., 2013. Effective conductivity and permittivity of unsaturated porous materials in the frequency range 1 mHz-1GHz, *Water Resources Research*, 49(1), 306–327.

Revil, A., Binley, A., Mejus, L., Kessouri, P., 2015. Predicting permeability from the characteristic relaxation time and intrinsic formation factor of complex conductivity spectra, *Water Resources Research*, 51(8), 6672–6700.

Revil, A., Cathles Iii, L. M., 1999. Permeability of shaly sands, *Water Resources Research*, 35(3), 651–662.

Revil, A., Eppehimer, J. D., Skold, M., Karaoulis, M., Godinez, L., et al., 2013. Low-frequency complex conductivity of sandy and clayey materials, *Journal of Colloid and Interface Science*, 398, 193–209.

Revil, A., Florsch, N., 2010. Determination of permeability from spectral induced polarization in granular media, *Geophysical Journal International*, 181(3), 1480–1498.

Revil, A., Karaoulis, M., Johnson, T., Kemna, A., 2012a. Some low-frequency electrical methods for subsurface

characterization and monitoring in hydrogeology, *Hydrogeology Journal*, 20(4), 617–658.

Revil, A., Koch, K., Holliger, K., 2012b. Is it the grain size or the characteristic pore size that controls the induced polarization relaxation time of clean sands and sandstones?, *Water Resources Research*, 48(5), 1–7.

Riedel, M., Collett, T. S., Hyndman R. D., 2005. Gas hydrate concentration estimates from chlorinity, electrical resistivity and seismic velocity, *Geological Survey of Canada*, *Open File*, 4934, 1–36.

Riedel, M., Collett, T. S., Kim, H. S., Bahk, J. J., Kim, J. H., et al., 2013. Large-scale depositional characteristics of the Ulleung Basin and its impact on electrical resistivity and Archie-parameters for gas hydrate saturation estimates, *Marine and Petroleum Geology*, 47, 222–235.

Riedel, M., Long, P. E., Collett T. S., 2006. Estimates of in situ gas hydrate concentration from resistivity monitoring of gas hydrate bearing sediments during temperature equilibration, *Marine Geology*, 227, 215–225.

Sahu, C., Kumar, R., Sangwai, J. S., 2020. Comprehensive review on exploration and drilling techniques for natural gas hydrate reservoirs, *Energy & Fuels*, 34(10), 11813–11839.

Santamarina, J. C., Dai, S., Terzariol, M., Jang, J., Waite, W. F., et al., 2015. Hydro-bio-geomechanical properties of hydrate-bearing sediments from Nankai Trough, *Marine and Petroleum Geology*, 66(2), 434–450.

Schmutz, M., Revil, A., Vaudelet, P., Batzle, M., Viñao, P. F., et al., 2010. Influence of oil saturation upon spectral induced polarization of oil-bearing sands, *Geophysical Journal International*, 183(1), 211–224.

Sen, P. N., Goode, P. A., 1992. Influence of temperature on electrical conductivity on shaly sands, *Geophysics*, 57(1), 89–96.

Shankar, U., Riedel, M., 2011. Gas hydrate saturation in the Krishna–Godavari basin from P-wave velocity and electrical resistivity logs, *Marine and Petroleum Geology*, 28(10), 1768–1778.

Shepard, F.P., 1954. Nomenclature based on sand-silt-clay ratios, *Journal of Sedimentary Petrology*, 24, 151–158.

Shi, K., Wei, R., Guo, X., Li, Q., Lv, X., et al., 2021. Enhancing gas production from hydrate-bearing reservoirs through depressurization-based approaches: knowledge from laboratory experiments, *Energy & Fuels*, 35(8), 6344–6358.

Sriram, G., Dewangan, P., Ramprasad, T., 2014. Modified effective medium model for gas hydrate bearing, clay-dominated sediments in the Krishna–Godavari Basin, *Marine and petroleum geology*, 58, 321–330.

Sun, Y., Wu, S., Dong, D., Lüdmann, T., Gong, Y., 2012. Gas hydrates associated with gas chimneys in fine-grained sediments of the northern South China Sea, *Marine Geology*, 311, 32–40.

Ta, X. H., Yun, T. S., Muhunthan, B., Kwon, T. H., 2015. Observations of pore-scale growth patterns of carbon dioxide hydrate using X-ray computed microtomography, *Geochemistry, Geophysics, Geosystems*, 16(3), 912–924.

Tarasov, A., Titov, K., 2013. On the use of the Cole-Cole equations in spectral induced polarization, *Geophysical Journal International*, 195(1), 352–356.

Waite, W. F., Santamarina, J. C., Cortes, D. D., Dugan, B., Espinoza, D. N., et al., 2009. Physical properties of hydrate-bearing sediments, *Reviews of Geophysics*, 47(4), 1–38.

Wang, X., Hutchinson, D. R., Wu, S., Yang, S., Guo, Y., 2011a. Elevated gas hydrate saturation within silt and silty clay sediments in the Shenhu area, South China Sea, *Journal of Geophysical Research: Solid Earth*, 116, B05102.

Wang, X., Wu, S., Lee, M., Guo, Y., Yang, S., et al., 2011b. Gas hydrate saturation from acoustic impedance and resistivity logs in the Shenhu area, South China Sea, *Marine and Petroleum Geology*, 28(9), 1625–1633.

Waxman, M. H., Smits, L. J. M., 1968. Electrical conductivities in oil-bearing shaly sands, *Society of Petroleum Engineers Journal*, 8(2), 107–122.

Wei, W. N., Li, B., Gan, Q., Li, Y. L., 2022. Research progress of natural gas hydrate exploitation with $CO_2$ replacement: A review, *Fuel*, 312, 122873.

Worthington, P. F., Collar, F. A., 1984. Relevance of induced polarization to quantitative formation evaluation, *Marine & Petroleum Geology*, 1(1), 14–26.

Wu, P., Li, Y., Wang, L., Wang, L., Sun, X., et al., 2021. Triaxial tests on the overconsolidated methane hydrate-bearing clayey-silty sediments. *Journal of Petroleum Science and Engineering*, 206, 109035.

Wu, P., Li, Y., Wang, L., Sun, X., Wu, D., et al., 2022. Hydrate-bearing sediment of the South China Sea: Microstructure and mechanical characteristics. *Engineering Geology*, 307, 1096782.

Xing, L., Niu, J., Zhang, S., Cao, S., Wang, B., et al., 2022. Experimental study on hydrate saturation evaluation

based on complex electrical conductivity of porous media, *Journal of Petroleum Science and Engineering*, 208, 109539.

Xing, L., Qi, S., Xu, Y., Wang, B., Lao, L., et al., 2021. Numerical study on complex conductivity characteristics of hydrate-bearing porous media, *Journal of Natural Gas Science and Engineering*, 95, 104145.

Yang, L., Zhao, J., Liu, W., Li, Y., Yang, M., et al., 2015. Microstructure observations of natural gas hydrate occurrence in porous media using microfocus X-ray computed tomography, *Energy & Fuels*, 29(8), 4835–4841.

Yang, M., Zhao, J., Zheng, J. N., Song, Y., 2019. Hydrate reformation characteristics in natural gas hydrate dissociation process: A review, *Applied Energy*, 256, 113878.

Ye, J. L., Qin, X. W., Xie, W. W., Lu, H. L., Ma, B. J., et al., 2020. The second natural gas hydrate production test in the South China Sea, *China Geology*, 3(2), 197–209.

Yin, Z., Linga, P., 2019. Methane hydrates: a future clean energy resource. *Chinese Journal of Chemical Engineering*, 27, 2026–2036.

Yun, T. S., Santamarina, J. C., Ruppel, C., 2007. Mechanical properties of sand, silt, and clay containing tetrahydrofuran hydrate, *Journal of Geophysical Research: Solid Earth*, 112, B04106.

Zhan, L., Wang, Y., Li, X. S., 2018. Experimental study on characteristics of methane hydrate formation and dissociation in porous medium with different particle sizes using depressurization, *Fuel*, 230, 37–44.

Zhu, Y., Wang, P., Pang, S., Zhang, S., Xiao, R., 2021. A review of the resource and test production of natural gas hydrates in China, *Energy & Fuels*, 35(11), 9137–9150.

Zhang, Z., Liu, L., Li, C., Cai, J., Ning, F., et al., 2021. Fractal analyses on saturation exponent in Archie's law for electrical properties of hydrate-bearing porous media, *Journal of Petroleum Science and Engineering*, 196, 107642.



https://dspace.org/

# Pore-scale modelling on complex-conductivity responses of hydrate-bearing clayey sediments: implications for evaluating hydrate saturation and clay content

**Xing, Lanchang; Zhang, Huanhuan; Wang, Shuo; Wang, Bin; Lao, Liyun ...**

**2023-02-01**
Elsevier
https://doi.org/10.1016/j.geoen.2022.211356
Xing L, Zhang H, Wang S, et al., (2023) Pore-scale modelling on complex-conductivity responses of hydrate-bearing clayey sediments: implications for evaluating hydrate saturation and clay content. Geoenergy Science and Engineering, Volume 221, February 2023, Article number 211356

Downloaded from a DSpace repository. https://dspace.org/